Optimization of processing parameters in the preparation of hematite thin films for photoelectrochemical water splitting

By

Adiel Holtzhausen

Submitted in partial fulfilment of the requirements
for the degree
Magister Scientiae (MSc) in Physics
in the
Faculty of Natural and Agricultural Sciences
Department of Physics
University of Pretoria

Supervisor: Prof MM Diale
Co-supervisor: Dr N Nombona

January 2022

Declaration

I, **Adiel Holtzhausen**, declare the following**:**

1. I understand what plagiarism entails and am aware of the University's policy in this regard.
2. I declare that this dissertation is my own, original work. Where someone else's work was used (whether from a printed source, the Internet or any other source) due acknowledgement was given and reference was made according to departmental requirements.
3. I did not copy and paste any information directly from an electronic source (e.g., a web page, electronic journal article or CD ROM) into this document.
4. I did not make use of another student's previous work and submitted it as my own.
5. I did not allow and will not allow anyone to copy my work with the intention of presenting it as his/her own work.

Signature: ______________________________

Date: 20 January 2022

Student number: 12115429

Abstract

In this study, the influence of coating techniques and layering of hematite (α-Fe_2O_3) thin films were studied. Two colloidal-based coating techniques namely dip coating and thermal spray pyrolysis were used to synthesize nanostructured hematite thin films. All films were annealed at 500 °C for I hr to perform the calcination from ɣ- Fe_2O_3 (magnetite) to α-Fe_2O_3 (hematite).

X-ray diffraction confirmed the calcination to hematite, it furthermore confirmed the hexagonal corundum structure of hematite. Raman spectroscopy confirmed the polycrystallinity of hematite with seven optical vibrational modes (two E_g and five A_{1g}) observed in the first Brillouin zone. Ultraviolet-visible spectroscopy showed good absorbance in the visible region with absorbance onset ranging from 596.75 – 608.75 nm. Scanning electron microscopy depicted various nanoparticles ranging from agglomerated nanodiscs and nanorods to nanospheres. This study showed that coating techniques could attribute to the optical and structural properties of hematite thin films for photoelectrochemical water splitting. Furthermore, a modified annealing approach was used to determine the effects of annealing time and multiple layer formation on the structural, optical and electronic properties of hematite thin films. Scanning electron microscopy revealed an increase in film thickness with increased annealing time. Furthermore, it depicted the formation of four single layers when annealing between each coating. UV-Vis indicated a decrease in bandgap with prolonged annealing. Additionally, UV-Vis revealed better absorption for coherent layers when compared to the single layers annealed four times. The photocurrent increased two-fold from 1.65 x 10^{-4} Acm^{-2} to 4.77 x 10^{-4} Acm^{-2} when annealing time was increased from 30 mins to 1 hr. Similarly, a significant improvement from 2.26 x 10^{-4} Acm^{-2} to 4.35 x 10^{-4} Acm^{-2} was found with a decrease of multiple layer formation and annealing frequency. From this work it was determined that annealing time and multiple layer formation by increased annealing frequency influences the optical, structural and electrical properties of nanostructured hematite thin films.

List of Abbreviations

PEC	Photoelectrochemical
STH	Solar-to-Hydrogen
CB	Conduction band
VB	Valence band
DFT	Density functional theory
UV	Ultraviolet
PTC	Photon to current
FTO	Fluorine doped tin oxide
XRD	X-ray diffraction
UV-Vis	Ultraviolet-visible
FE-SEM	Field Emission scanning electron microscopy
M-S	Mott Schottky
LSV	Linear scan voltammetry
FWHM	Full width at half maximum
RHE	Reversible hydrogen electrode
AGI	Average grain intercept
DC	Dip coating
SP	Spray pyrolysis
1L_1hr	One layer annealed once for 1 hr
4CL_1hr	Four coherent layers annealed once for 1 hr

4SL_1hr	Four single layers annealed once between each layer formation

Dedication

This work is the fruit of many hours of work and sacrifice. To my grandfather Andre Stephanus Kruger, grandmother Lettie Kruger and my wonderful parents Alta and Maj.Genl Deon Holtzhausen who supported, prayed and sacrificed so much for my dreams.

Psalm 46

Acknowledgements

Firstly, I would like to thank God for His grace and strength during my research project. Without His guidance, I would not have achieved much.

I would like to express my sincere gratitude to Prof. Mmantsae M. Diale for her supervision, tremendous support, guidance and encouragement during my masters degree. Her leadership and teachings have taught me invaluable lessons for which I will always be grateful.

I would like to thank Dr. Nolwazi Nombona for her continued advice and guidance with regards to chemical compounds.

I would additionally like to thank the Clean and Green energy group for their continued support, advice and constructive criticism. The group provided a space for facilitated learning and discussion. Additionally, I would like to thank Dr. Justine Nyarige for taking the time to show me the principles of spray pyrolysis along with the inner workings of characterization.

I acknowledge the Physics Department along with Prof. Chris Theron, the Head of Physics at the University of Pretoria.

I would also like to thank the microscopy team at the University of Pretoria for their contribution to my understanding of FEG-SEM and microscopy.

A special thanks to the National Research Foundation (NRF), NoN0115/115463 (SARChI, M.D.) for their financial contribution.

Finally, I would like to thank my family for their continued encouragement, love, support and endless patience during my studies.

Table of Contents

List of Figures

List of Tables

1 Introduction

1.1 Rationale

The demand for clean energy has been increasing due to the limitations of fossil fuels. These limitations are mainly attributed to population growth, pollution and industrialization. Photoelectrochemical (PEC) water splitting for hydrogen fuel production has been increasingly reported as a mean of clean energy, since 1972. Solar irradiation is used to split the water molecules into oxygen (O_2) and hydrogen (H_2) which is then stored as chemical energy and used as a clean fuel.

Fujishima and Honda were the first to report on successful PEC water splitting in 1972, using titanium dioxide (TiO_2) photoanode [1]. However, due to the large bandgap of TiO_2, a low efficiency of 0.1 % was reported [1]. Since then, other semiconductors with smaller bandgaps, such as tungsten trioxide (WO_3) [2], zinc oxide (ZnO) [3], cadmium selenide (CdSe) [4] and hematite (α-Fe_2O_3) [5] have been researched.

Among these, cadmium selenide is a good candidate due to the suitable bandgap of 1.7 eV [6]. Moreover, it has favourable band edges located at ~ -6.8 eV and ~-4.8 eV for the valence and conduction bands [7]. This makes cadmium selenide a prospective photocatalytic semiconductor as it is able to drive both the oxygen and hydrogen evolution. However, cadmium selenide suffers from high recombination rates along with photocorrosion [8]. Tungsten trioxide has been reported as a promising photoanode due to a suitable bandgap of 2.6 eV and high valence band location [6]. Furthermore, tungsten trioxide can perform the oxidation half reaction but due to the low position of the conduction band, it cannot perform the reduction half reaction. Similarly, tungsten trioxide suffers from low photocurrent efficiencies [2]. Zinc oxide has been reported as a photoanode and photocathode for water splitting. The conduction band and valence band edges straddle both the hydrogen and oxygen evolutions [6]. Thus, zinc oxide could potentially drive both the oxidation and reduction potentials. However, zinc oxide has yielded low photocurrent and efficiency which is attributed to the relatively large bandgap of 3.2 eV. Similar metal oxide semiconductors such as copper(I)oxide (Cu_2O) [9] and hematite (α-Fe_2O_3) [10] have been reported on for PEC water splitting.

Among these, Hematite (α-Fe_2O_3) is one of the most promising semiconductors. This is due to its favourable bandgap of 1.9 – 2.2 eV which allows for a 40 % absorption of the solar spectrum [11, 12]. Hematite has been reported with solar to hydrogen efficiencies ranging up to 16.8 % [13-15]. Additionally, the valence band edge is situated low enough to drive the oxygen evolution efficiently. Furthermore, hematite offers high stability in aqueous solutions, abundance, cost efficiency and non-toxicity. However, α-Fe_2O_3 has some associated limitations such as high recombination rates due to short excitation lifetimes of 3–10 ps and the limited charge carrier mobility of <1 $cm^2V^{-1}s^{-1}$ which leads to low conductivity [14, 16-18]. These limitations can be improved by various approaches such as doping, nanostructuring, anodization and layering [19-21].

1.2 Layering hematite thin films

The synthesis of hematite nanoparticles by various coating techniques for PEC water splitting such as dip coating, spray pyrolysis, electrodeposition and spin coating have been reported to form different nanoparticle shapes such as nanodiscs [22], nanorods [23] and nanospheres [24]. However, many of these techniques have yet to be directly compared. In this study we directly compared the influence of dip coating and spray pyrolysis on the structural and optical properties of hematite. A variation in the annealing time for hematite thin film synthesis has been reported to affect the structural and electrical properties of hematite thin films [25]. Thus, we proposed studying the influence of annealing time from 30 mins to 1 hr on the structural and optical properties of hematite. The influence of layer formation due to annealing frequency has yet to be reported on. In this study the layering of samples with a modified annealing approach was studied to describe the effect on the optical, structural, and electrical properties.

1.3 Aims and objectives

This study aims to investigate the influence of coating and annealing techniques to synthesize and characterize hematite nanoparticles for PEC water splitting. The main objectives are the following:

- Structural and optical properties of hematite thin films prepared by dip coating and spray pyrolysis.
- Influence of annealing time on the structural, optical, and electrical properties of hematite nanoparticles.
- Influence of layering due to annealing frequency on the structural, optical, and electrical properties of α-Fe_2O_3 thin films for PEC water splitting.

1.4 Dissertation Structure

This dissertation is outlined as follows: In chapter 2, we present the background information, workings of a PEC cell, requirements of the material, workings, and motivation of the research. Chapter 3 discusses the experimental methods, coating techniques employed and characterization of the α-Fe_2O_3 thin films. Chapter 4 presents the results obtained from the experiments performed. Chapter 5 concludes the work and furthermore recommends future work.

References

[1] Fujishima, A. and K. Honda, *Electrochemical photolysis of water at a semiconductor electrode.* nature, 1972. **238**(5358): p. 37-38.

[2] Hodes, G., D. Cahen, and J. Manassen, *Tungsten trioxide as a photoanode for a photoelectrochemical cell (PEC).* Nature, 1976. **260**(5549): p. 312-313.

[3] Patel, P.P., et al., *Nitrogen and cobalt co-doped zinc oxide nanowires–Viable photoanodes for hydrogen generation via photoelectrochemical water splitting.* Journal of Power Sources, 2015. **299**: p. 11-24.

[4] Ellis, A.B., S.W. Kaiser, and M.S. Wrighton, *Optical to electrical energy conversion. Characterization of cadmium sulfide and cadmium selenide based photoelectrochemical cells.* Journal of the American Chemical Society, 1976. **98**(22): p. 6855-6866.

[5] Krishnakumar, R., et al., *Thin film preparation by spray pyrolysis for solar cells.* Materials chemistry and physics, 1987. **16**(5-6): p. 385-395.

[6] Gellé, A. and A. Moores, *Water splitting catalyzed by titanium dioxide decorated with plasmonic nanoparticles.* Pure and Applied Chemistry, 2017. **89**(12): p. 1817-1827.

[7] Riley, E.A., C.M. Hess, and P.J. Reid, *Photoluminescence intermittency from single quantum dots to organic molecules: Emerging themes.* International journal of molecular sciences, 2012. **13**(10): p. 12487-12518.

[8] Yu, X.-Y., et al., *High performance and reduced charge recombination of CdSe/CdS quantum dot-sensitized solar cells.* Journal of Materials Chemistry, 2012. **22**(24): p. 12058-12063.

[9] Jian, J. and J. Sun, *A Review of Recent Progress on Silicon Carbide for Photoelectrochemical Water Splitting.* Solar RRL, 2020. **4**(7): p. 2000111.

[10] Maabong, K., et al., *Nanostructured hematite thin films for photoelectrochemical water splitting.* Physica B: Condensed Matter, 2018. **535**: p. 67-71.

[11] Dias, P., et al., *Extremely stable bare hematite photoanode for solar water splitting.* Nano Energy, 2016. **23**: p. 70-79.

[12] Kim, D.H., et al., *Vertically ordered hematite nanotube array as an ultrasensitive and rapid response acetone sensor.* ACS applied materials & interfaces, 2014. **6**(17): p. 14779-14784.

[13] Simfukwe, J., et al., *Exploring the stability and electronic properties of Zn-doped hematite surfaces for photoelectrochemical water splitting.* Journal of Physics and Chemistry of Solids, 2020. **136**: p. 109159.

[14] Mirbagheri, N., et al., *Visible light driven photoelectrochemical water oxidation by Zn-and Ti-doped hematite nanostructures.* Acs Catalysis, 2014. **4**(6): p. 2006-2015.

[15] Le Formal, F., M. Grätzel, and K. Sivula, *Controlling photoactivity in ultrathin hematite films for solar water-splitting.* Advanced Functional Materials, 2010. **20**(7): p. 1099-1107.

[16] Sivula, K., F. Le Formal, and M. Grätzel, *Solar water splitting: progress using hematite (α-Fe2O3) photoelectrodes.* ChemSusChem, 2011. **4**(4): p. 432-449.

[17] Tamirat, A.G., et al., *Using hematite for photoelectrochemical water splitting: a review of current progress and challenges.* Nanoscale Horizons, 2016. **1**(4): p. 243-267.

[18] Barroso, M., et al., *Charge carrier trapping, recombination and transfer in hematite (α-Fe 2 O 3) water splitting photoanodes.* Chemical Science, 2013. **4**(7): p. 2724-2734.

[19] Steier, L., et al., *Understanding the role of underlayers and overlayers in thin film hematite photoanodes.* Advanced Functional Materials, 2014. **24**(48): p. 7681-7688.

[20] Subramanian, A., et al., *Trade-off between Zr passivation and Sn doping on hematite nanorod photoanodes for efficient solar water oxidation: effects of a ZrO2 underlayer and FTO deformation.* ACS Applied Materials & Interfaces, 2016. **8**(30): p. 19428-19437.

[21] Wang, D., et al., *Enhanced photoelectrochemical water splitting on hematite thin film with layer-by-layer deposited ultrathin TiO2 underlayer.* International journal of hydrogen energy, 2014. **39**(28): p. 16212-16219.

[22] Lu, J., et al., *Hematite nanodiscs exposing (001) facets: synthesis, formation mechanism and application for Li-ion batteries.* Journal of Materials Chemistry A, 2013. **1**(17): p. 5232-5237.

[23] Morrish, R., et al., *Activation of hematite nanorod arrays for photoelectrochemical water splitting.* ChemSusChem, 2011. **4**(4): p. 474-479.

[24] Nyarige, J.S., T.P. Krüger, and M. Diale, *Effects of L-arginine concentration on hematite nanostructures synthesized by spray pyrolysis and chemical bath deposition.* Physica B: Condensed Matter, 2020. **581**: p. 411924.

[25] Li, L., et al., *The effect of annealing regime and electrodeposition time on morphology and photoelecrochemical performance of hematite converted from nanosheet γ-FeOOH.* Journal of Photochemistry and Photobiology A: Chemistry, 2019. **369**: p. 8-15.

2 Hematite-based photoanodes for photoelectrochemical water splitting

2.1 Introduction

Photoelectrochemical (PEC) water-splitting is a solar-to-hydrogen (STH) technique that has been widely researched since 1972. The process requires semiconductors as light absorbers, with hematite being the material used in this dissertation. Hematite is chosen because it has a small bandgap which absorbs light in the visible spectrum leading to a good theoretical solar-to-hydrogen (STH) efficiency of up to 15%. This chapter describes the working principle of PEC water splitting, the basic requirements of semiconductors used for water splitting, the crystal structure of hematite, along with optimization techniques for hematite conductivity such as nanostructuring and preparation methods.

2.2 PEC water splitting

Fujishima and Honda were the first to report on the PEC water-splitting in 1972. They used a titanium dioxide (TiO_2) photoanode connected to a platinum (Pt) cathode [1, 2]. Titanium dioxide was considered a favourable material for PEC water-splitting due to its abundance, stability in aqueous mediums and low relative cost. It does however fall short due to its large bandgap of 3.2 eV, absorbing sunlight only in the small ultraviolet (UV) region. In their study, UV light was irradiated on the titanium dioxide (TiO_2) photoanode, as illustrated in Figure 2.1, and it generates the electron-hole pairs which initiated the water-splitting reaction. The water got oxidized to oxygen (O_2) with the formation of hydrogen ions (H^+). The H^+ was eventually reduced at the cathode to produce hydrogen (H_2). The H_2 yield for this experiment was estimated at 0.1% [1].

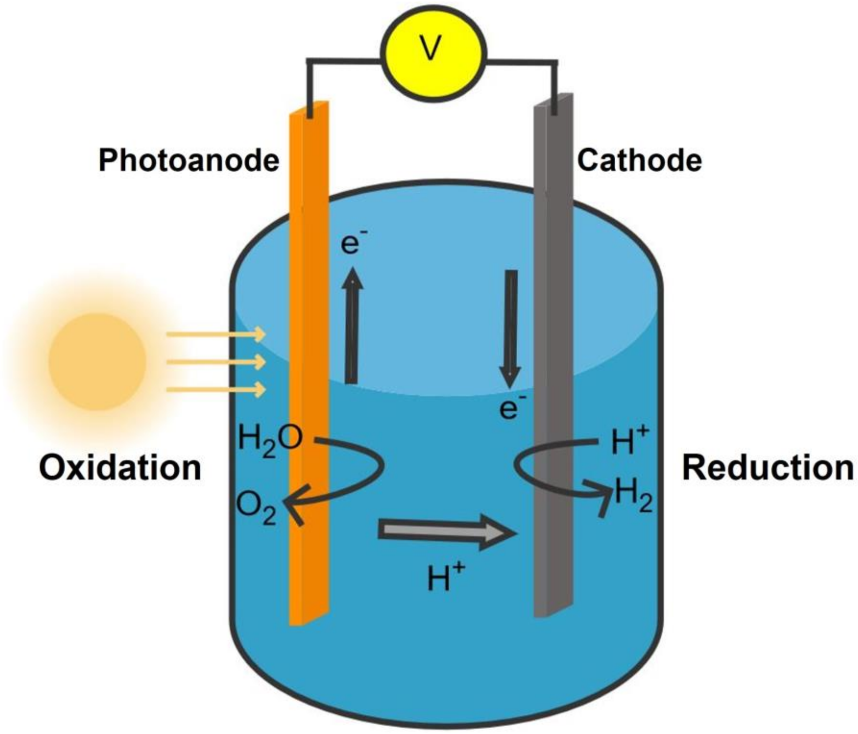

Figure 2.2.1. Illustration of a photoelectrochemical cell, where reduction takes place at the cathode and oxidation at the photoanode.

Since then, various semiconductors have been extensively studied as possible photocathode and photoanodes. There are a few prerequisites for these semiconductor materials to be used as light absorbers, which is primarily attributed to abundance, low cost, stability in aqueous mediums, non-toxicity, carbon neutrality, and favourable bandgap properties [3]. The valence band and conduction band positions play a large role in PEC water-splitting. The valence band of a semiconductor needs to be below the H_2O/O_2 potential to drive the oxidation evolution to produce oxygen whereas the conduction band needs to be above the H_2/H_2O potential to drive the reduction evolution of the redox reaction. Figure 2.2.1 illustrates the PEC cell which consist of a light absorbing semiconductor (working electrode), a counter electrode, and a reference electrode. Under illumination the semiconductor will absorb light with an energy greater than its bandgap.

This gives rise to the electron-hole pairs which are subsequently used as charge carriers. A charge depletion region is then formed at the interface between the semiconductor and the electrolyte. Due to the electric field inside this depletion region, the electrons-hole pairs are then separated. The electrons are drawn to the conduction band and travel to the back contact after which they are transported by means of an external bias to the cathode where they drive the water reduction reaction. The holes travel to the semiconductor/electrolyte interface where they drive the oxidation reaction. PEC water-splitting consists of two redox half-reactions as follows:

Water reduction half-reaction [4]:

$$2H^+ + 2e^- \rightarrow H_2 \qquad E^0_{H^+/H_2O} = 1.23V \tag{1}$$

Water oxidation half-reaction:

$$2H_2O + 4h^+ \rightarrow 4H^+ + O_2 \quad E^0_{H^+/H_2} = 0V \tag{2}$$

Full redox equation:

$$2H_2O \rightarrow 2H_2 + O_2 \tag{3}$$

[4]

where h^+ denotes the holes, e^- denotes the electrons and E^o denotes the potential needed for the water splitting redox reaction [4]. Under standard conditions the change in free energy, or the Gibbs free energy (ΔG^o) for the water-splitting redox reaction is 237.2 kJ·mol^{-1}, which, by the Nernst equation (equation 5) corresponds to a redox potential (ΔE^o) of 1.23 V per electron. From these values, it can be concluded that the semiconductor material used for water-splitting should absorb light with a photon energy greater than 1.23 eV [4]. However, due to the high energy losses of the evolution overpotential, a more realistic bandgap energy of ~1.4 to 2.25 eV is needed for water-splitting. The Nernst equation is presented as follows:

$$E = E^0 - \frac{RT}{zF} \ln Q \qquad 5$$

where E denotes the reduction potential, E^0 denotes the standard potential, R denotes the universal gas constant, T denotes the temperature, z denotes the mole ion charge, F denotes the Faraday constant and Q denotes the reaction quotient.

Figure 2.2.2 illustrates some of the studied semiconductor materials used to drive water-splitting. It can be seen that only a few materials have viable bandgaps to perform both the reduction and oxidation half-reactions. Semiconductors which can perform both redox reactions are gallium phosphide (GaP) [5] , cadmium selenide (CdSe) [6], cadmium sulfide (CdS) [7], zinc oxide (ZnO) [8], titanium dioxide (TiO_2) [9] and silicon carbide (SiC) [10] of which all have a large bandgap except for CdSe and CdS which show high recombination rates and photocorrosion [11]. Iron pyrite (FeS_2) [12] can perform the hydrogen evolution due to its favourable conduction band position yet, is unable to perform the oxygen evolution as the valence band is positioned too high. The limitation of FeS_2 was only discovered in 2014 by Jin *et al* as hole-traps which are caused by bulk defect states of a missing sulphur (S) atom, this causes low photovoltage [13]. Hematite (Fe_2O_3) [14], tungsten trioxide (WO_3) [15] and tin dioxide (SnO_2) [16] can perform the oxygen oxidation evolution, yet their conduction bands are positioned too low to perform the hydrogen evolution. Fe_2O_3, WO_3, and SnO_2 have different limitations, namely; fast recombination rates, high photocorrosion and wide bandgap, respectively.

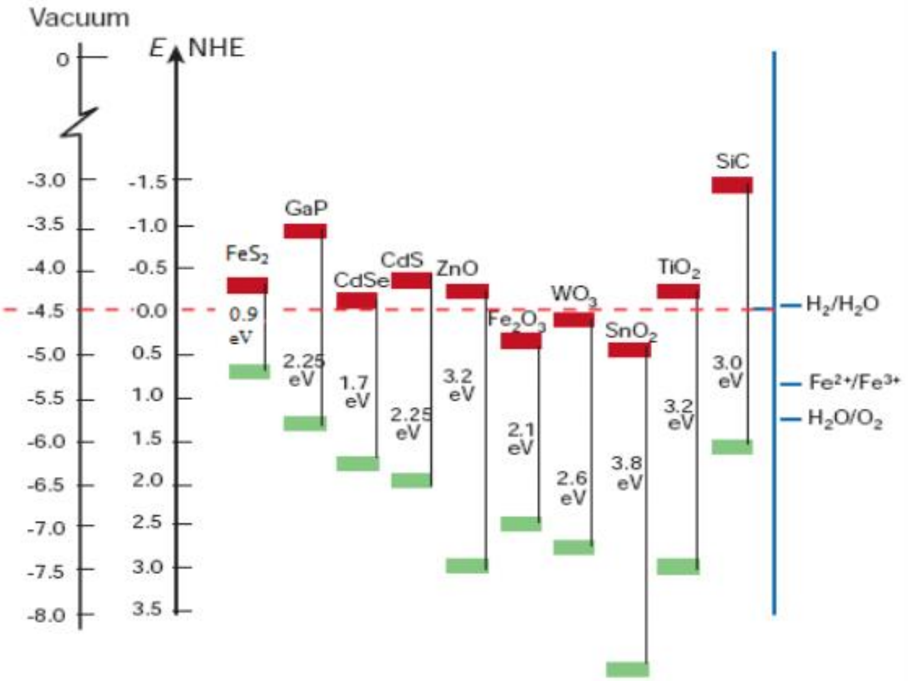

Figure 2.2.2. Band edge positions of semiconductor materials submerged in aqueous solution with an electrolyte of pH 1 [17].

2.3 Basic requirements of semiconductor materials for PEC water splitting

As mentioned previously in an ideal system a bandgap energy of 1.23 eV is needed to drive the hydrogen and oxygen evolution (however, this is not the practical case). The band potential plays an important role in the efficiency of a semiconductor used for PEC water-splitting. Figure 2.3.1 illustrates a semiconductor in aqueous medium of pH 1, with viable conduction and valence band positions. The energy scale on the left is comparable to that of a hydrogen electrode in vacuum. It is noteworthy to mention that the pH can potentially affect semiconductor band edges.

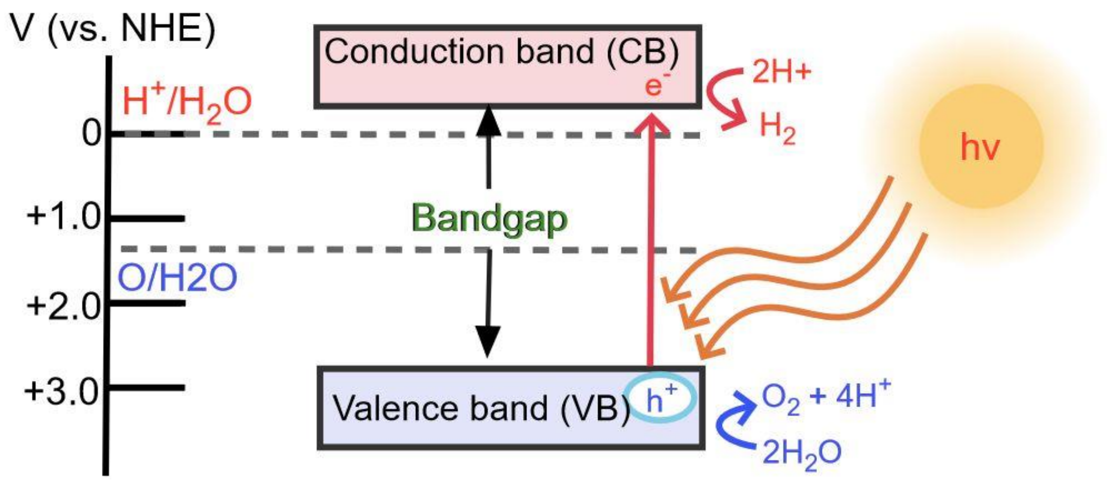

Figure 2.3.1. Energy diagram of a suitable semiconductor to drive the redox reactions for PEC water-splitting.

There are six main factors by which a semiconductor should be measured to determine its viability as a photoanode. These are [18]:

(i) Visible light absorption: The light-absorbing region for a semiconductor is determined by the energy of its bandgap. For ideal water-splitting an energy of 1.23 eV would be required, however in experimental procedures more energy is needed due to heat transfer and thermodynamic losses [19, 20]. From figure 2.3.2, it is observed that sunlight falls immensely under 0.38 μm which correlates to 3 eV and thus absorption below this point would only adhere to a very small portion of the solar spectrum. This means that for ideal solar absorption a semiconductor needs a bandgap of between 1.9 eV and 3.0 eV. The theoretical maximum efficiency for a perfect material with a bandgap of 2.03 eV would be 16.8%. However, efficiency can be improved by making use of tandem solar cells, where more than one semiconductor is used [21].

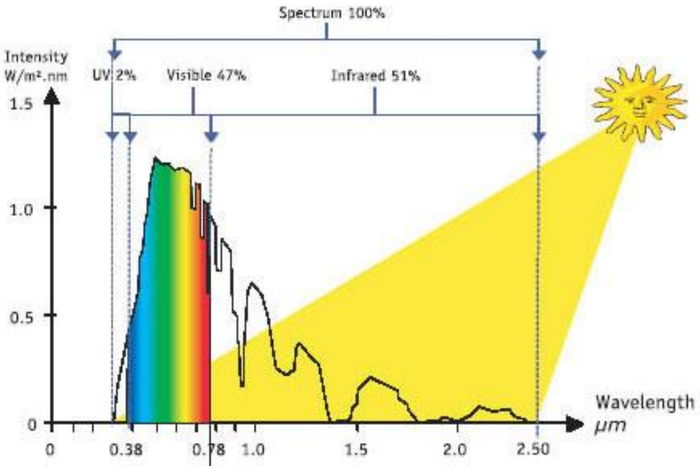

Figure 2.3.2. Intensity of sunlight versus wavelength of the light spectrum, the coloured section between 0.38 µm and 0.78 µm represents the visible spectra [22].

(ii) Chemical stability in aqueous solutions: High chemical stability is needed in alkaline aqueous solutions for both light and dark phases. Traditionally, semiconductor metal oxides that have larger bandgaps are known to be more stable in aqueous solution under varying light conditions. Stability can be increased by making use of dopants as well as variating the pH and stoichiometry [23].

(iii) Favourable band edge positions to drive redox reactions: For a semiconductor to drive the water-splitting redox half-reactions (shown in figure 2.3.2), the conduction band edge of the semiconductor needs to be above the reduction potential, whereas the valence band edge of the semiconductor needs to be below the oxidation potential. Most semiconductor materials are only able to drive one of the two half-reactions, one of the solutions to this is by making use of tandem cells.

(iv) High charge mobility in the semiconductor material: Charge transport is an important aspect when it comes to conductivity and efficiency. When recombination rates are high, the water-splitting efficiency will be lower due to ineffective electron charge transfer or conductivity. These contributes to the low conversion efficiencies in metal oxide photoanodes.

(v) Low overpotentials in the semiconductor for the redox reactions: At the interface between the metal oxide photoanode and the electrolyte, the charge transfer needs to be quick to limit them from piling up on the materials surface which leads to an increase in electron-hole recombination rates. Cocatalysts are commonly used to reduce efficiency losses due to slow charge transfer.

(vi) Low cost: Cost is a major factor in producing a renewable energy source. The materials used in a PEC cell must be cost efficient, natural or renewable and preferably non-toxic, to compete with other hydrogen producing systems.

Most of the above listed requirements are dependent on morphological factors such as crystallinity, structure and particle size [18]. Various studies have been done on improving the quality of semiconductors. This will be discussed more in section 2.5.

Currently no perfect semiconductor material exists, and thus various semiconductors are being extensively researched as possible solutions. Semiconductors can be approached from two mindsets, the first of which would be to explore materials with favourable water-splitting properties, whilst the second approach investigates various coating and growing techniques to improve already studied materials. Other possibilities include the usage of tandem cells and catalysts in a PEC device [24]. In this study hematite was explored as a possible semiconductor photoanode.

2.4 Hematite

Hematite (α-Fe_2O_3) has been identified as abundant and non-toxic material, making it favourable for widespread applications in solar cells, electronics, catalysts, pigments for paints and ink, cosmetics, mining, gas sensors, photoelectrode and anodes in Li-ion batteries. α-Fe_2O_3 is the most thermodynamically stable form of iron oxide, and stable in aqueous mediums which makes it ideal for PEC water-splitting. Hematite has a stable spinel structured oxide in the midst of the Fe^{2+} ion in octahedral positions and the Fe^{3+} ion in tetrahedral positions at room temperature, which links to an n-type semiconductor with a theoretical bandgap of 2.1 eV [25, 26]. The hematite unit cell consists of a hexagonal close-packed structure of oxygen atoms with iron atom interstices, which displaced two thirds of atoms from the octahedral sites. These lattices naturally arrange in the corundum structure where each iron atom has six neighbour oxygen atoms and conversely each oxygen atom has four neighbouring iron atoms. This forms the rhombohedral centered hexagonal hematite unit cell as shown in figure 2.4.1.

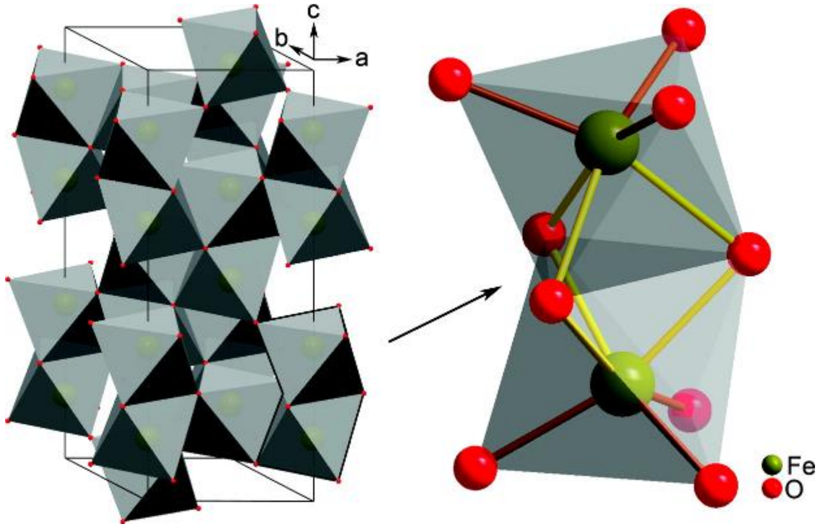

Figure 2.4.1. Crystalline structure for an α-Fe_2O_3 (hematite) unit cell [27].

According to various studies it was found that hematite has an indirect bandgap transition due to the Fe^{3+} d-d transition origin [28, 29]. Conversely few studies are reporting a direct bandgap which could be due to the charge transfer occurring between the 2p oxygen orbital and the 3d iron orbital with an energy greater than 3.2 eV [30, 31]. Hematite has a bandgap that ranges from 1.9 eV to 2.2 eV, which corresponds to a wavelength of 560 nm that falls in the visible region [32, 33]. The absorption range for this material ranges from yellow to ultraviolet and thus hematite mainly absorbs in the visible spectrum of the electromagnetic radiation [34]. Hematite has a reddish-brown/rust appearance as it transmits light in this spectrum. For hematite the conduction band can be calculated both theoretically as well as experimentally. DFT + U theoretical calculations showed that for the (0001) and (0112) points, the conduction band values were -4.48 eV and -5.34 eV respectively [4, 27]. Hankin *et al.* used a bandgap energy of 2.05 eV and reported that for an energy of 2.05 eV, the conduction and valence band energies for the (0001) and (0112) points were $E_{CB\,(0001)} = -3.46$ eV; $E_{VB\,(0001)} = -5.51$ eV and $E_{CB\,(0112)} = -4.32$ eV; $E_{VB\,(0112)} = -6.37$ eV respectively.

From this study it is reported that hematite reduces the water to hydrogen and oxygen. This is not normally the case for hematite, as it usually serve as the reducing agent (oxidises the water) as observed from Mott-Schottky and other experimental calculations [35]. The iron spin configuration influences the carrier transport along with the optical properties of hematite. Thus, the magnetic properties indirectly affects the PEC performance of hematite [4]. Hematite is known to transition from antiferromagnetic to weak ferromagnetic at room temperature [36].

The limitations of using hematite as a photoanode in PEC water splitting include its slow water oxidization time, short electron excitation lifetime and lengthy charge transport times. The latter of which causes photovoltage losses and quick electron-hole recombination rates which could potentially be detrimental to high photocurrent efficiency[37]. Also, due to the short hole diffusion length of hematite, thin films are preferred over bulk films as it helps to limit high recombination rates [38]. Thus, there have been numerous studies towards improving hematite thin films for PEC water splitting using coating techniques, doping and tandem junctions. These factors have been greatly studied since the 1980's and will be discussed in the next section.

2.5 Optimizing hematite conductivity

Hematite has many beneficial properties and is yet to be fully optimized as a photoanode. It has a bandgap of 1.9~2.1eV which correlates with its absorption in the visible region [39, 40]. This absorption region accounts for 40% of the solar spectrum [41]. Other benefits include abundance [4], thermodynamic stability in aqueous mediums [41] and low cost [42]. Hematite has a STH efficiency of 14-16% [43]. However, hematite has some limiting factors which includes low surface reaction rates [44], low charge carrier mobility[45] and high electron-hole recombination rates and short excitation lifetimes of 3-10 ps [45]. Additionally, the bandgap edges are positioned in such a manner that the valence band is suitable for oxygen evolution to take place, yet the conduction band is positioned too low to perform the hydrogen evolution reaction [46]. Thus, an external bias is required to produce hydrogen at the cathode as shown in figure 2.5.1.

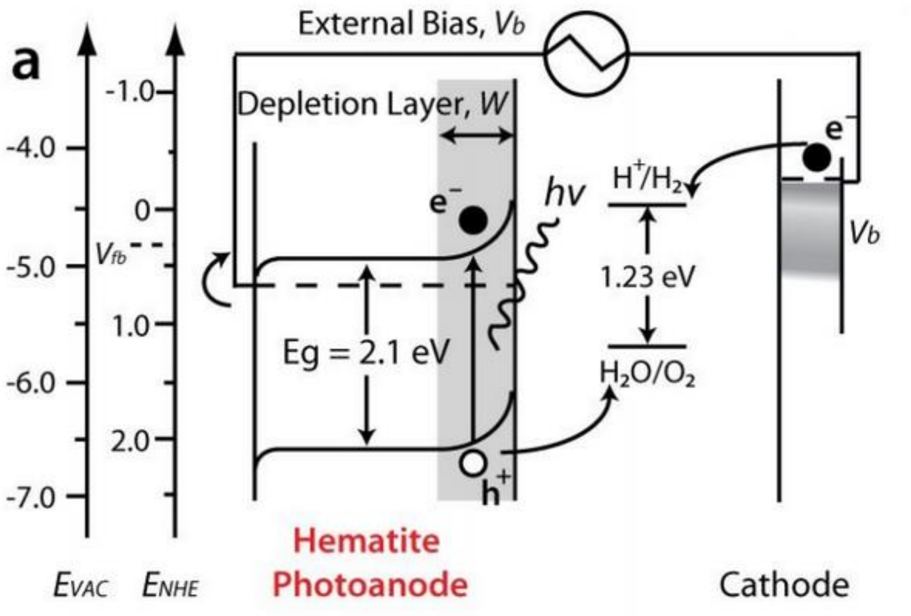

Figure 2.5.1. Energy diagram of a hematite photoanode in a PEC cell, where the anode drives the oxidation half-reaction, and the cathode drives the reduction half-reaction [4].

To address the problem of short excitation lifetime and low conductivity, researchers have resorted to nanostructured hematite, surface modification, heterojunction formation and doping [47].

2.6 Surface modification

Cocatalysts such as Co_3O_4 (cobalt tetraoxide) [48] , CoP (cobalt-phosphate) [49], NiFeOOH (nickel-iron (oxy)hydroxide) [50] and NiB (nickel-bromide) [51] have been used to enhance oxidation and reduce the onset potential, consequently increasing the efficiency of the PEC water-splitting for hematite. The high charge carrier recombination rates could be due to trapping sites at the surface of the semiconductor. This could possibly be corrected with the addition of over- and under-layers such as Al_2O_3 (aluminium trioxide) [52]. Under-layer materials are used to minimize electron-hole recombination by supressing the back flow of electrons from the conducting substrate, thus leading to an increase in photocurrent efficiencies [47]. Neufeld *et al.* found that the addition of an Al_2O_3 overlayer to nanostructured hematite led to a decrease in the overpotential, thereby increasing the photocurrent density [52]. Deng *et al.* observed that amorphous Fe_2TiO_5 (pseudobrookite) overlayers on TiO_2 demonstrated lower onset potential resulting in increased light-absorbance, and consequently enhancing the photocurrent [53]. However, even after these improvements the ideal hematite photoanode still has a low yield of ~12.6 $mA \cdot cm^{-2}$ [37, 54]. Furthermore, Paradzah *et al.* used Nb_2O_5 (niobium pentoxide) and SnO_2 (tin oxide) underlayers, which extended the short hole lifetimes, and found that there was a decrease in electron-hole pair recombination, as compared to pristine hematite [55]. Similarly Paradzah *et al.* also made use of elemental doped hematite with 15% Ti (titanium), which maximized its photocurrent efficiency to 1.83 $mA.cm^{-3}$, it was also found that doping with a higher percentage of Ti led to an overlayer of TiO_2 (titanium dioxide) forming, which reduced the photocurrent [55].

2.7 Doping

Doping is an improvement technique for PEC performance which could either be used alone or in combination with other techniques [56, 57]. Doping is used to increase carrier concentration which causes longer excitation lifetimes, thus increasing conductivity [58]. Elemental doping is used to increase carrier concentration which creates dopant energy levels in the host material, which causes a narrowed bandgap, and lead to increased absorption spectra in the semiconductor [59]. Gomathi *et al* noted that a red shift in the bandgap, towards the visible region occurred for TiO_2 samples doped with Zn^{2+} and V^{5+} [60]. The Zn^{2+} doped sample additionally showed enhanced photocatalytic activity and efficiency [60]. Dopants such as Cu (copper) [61], Zn (zinc) [62], Sn (tin) [63], P (phosphor) [64], Ti (titanium) [61], Ni (nickel) [65] and Pt (platinum) [66] have been used to enhance the PEC properties of hematite. Nyarige *et al.* doped hematite with L-arginine and found an increase in the photocurrent density from 1.6×10^2 mA.cm^{-3} for pristine hematite to 9.8×10^2 mA.cm^{-3}, for 1:3 ratio of hematite to L-arginine [67, 68]. Furthermore, DFT (density functional theory) calculation of Simfukwe *et al.* proved that doping Fe_2O_3 with Zn (zinc) and Cu (copper) increases the depletion charge from the Cu atom to the Fe and O atoms, thus reducing the distance travelled by the charge carriers. This leads to decreased electron-hole recombination which increases photoelectrochemical water oxidation and thus increased photocurrent. Similarly, doping with Zn lead to a decreased bandgap without recombination trap centres in the form of impurities [69, 70].

More so, a theoretical study performed by Liao *et al.* in 2011 suggested that doping α-Fe_2O_3 with Zr (zirconium), Si (silicon) or Ge (germanium) is superior to doping with Ti (titanium) as they do not act as electron trapping states [71]. Additionally, this study suggested that doping with Si showed superior electron transport activity due to strong covalent interactions between O and Si

[71]. The implication of this research was to promote covalent interactions between the oxygen and the dopant as this could yield to increased carrier transport, thus enhancing the electron mobility [64]. Simfukwe *et al.* co-doped Fe_2O_3 with bimetallic pairs namely Zn-Ti (zinc-titanium) and Zn-Zr (zinc-zirconium) found an increase in light absorption and charge carrier mobility from the valence band to the conduction band. This led to increased water oxidation activity and thus an improvement in photocurrent efficiencies [72]. Dopants with low bandgaps such as Si (silicon), Ti (titanium) and P (phosphor) have been reported to improve donor density, thus improving the photocurrent efficiency [73].

2.8 Heterojunctions

Heterojunctions are used to increase charge transport and light absorption. A heterojunction is the conjunction of two semiconductor materials with different properties. Heterojunctions can improve three aspects of PEC cells namely carrier efficiency, visible light absorption and electron-hole pair recombination [74]. In heterojunctions, the processes of light absorption and charge transport can take place in two different semiconductor materials [75]. Zhao *et al.* reported that WO_3/Fe_2O_3 n/n heterojunction nanostructures yielded lower onset potential, thus improving the PEC efficiency [76]. Similarly, Hsu *et al*. and Wang *et al*. reported on ZnO/Fe_2O_3 nanowires [77] and Fe_2O_3/TiO_2 heterojunctions respectively, both yielding lower onset potential and higher PEC efficiencies when compared to the pristine hematite.[78]. The observed improvements in the PEC efficiency were attributed to the reduction of charge recombination rates due to the heterojunction interface, leading to the improved photocurrent densities. Bassi *et al*. prepared a Fe_2O_3/Fe_2TiO_5 nanorod heterojunction which demonstrated increased photocurrent density and high surface charge separation of 85% efficiency at 1.32V operating voltage. An improvement in photocurrent performance was observed due to increased charge separation which was due to favourable band alignment [75]. Subsequently, heterojunctions can be used in combination with nanostructuring to improve the PEC performance of hematite.

2.9 Nanostructuring

Nanostructuring has been effectively used to improve the PEC water-splitting efficiency of hematite. Maabong *et al* used nanostructring and found that a decreased feature size will increase effective surface area. This led to improved charge separation, thus improving the conductivity of the hematite thin film [79].When employed correctly nanostructuring can aid the improvement of various limitations such as high recombination rates, short diffusion length, low absorption, and photon to current (PTC) efficiencies of hematite [80]. This improvement is due to an increased interfacial area between the photoelectrode and the electrolyte, which is favourable for enhanced PEC activity, such as lowered charge carrier mobility distance and charge separation [74]. Various nano shapes such as nanoflowers [81], nanorods [82], nanotubes [83], nanoflakes [84], nanodiscs [85], nanosheets [86], nanocones [87], and nanospheres [88] have been researched. In particular, one-dimensional nanostructures, such as nanotubes, nanorods and nanowires have been shown to enhance light absorption and to decrease charge carrier distance between the semiconductor and the electrolyte [80, 89]. Both Zhang *et al*. and Mao *et al*. reported an increased PEC efficiency due to the formation of hematite nanotubes [90, 91]. Nanostructuring was also reported to increase efficiencies of photoelectrodes. Mao *et al*. reported on the influences of nanotubes and nanorods by the electrodeposition coating method. They found that nanotubes performed better than nanorods for PEC water-splitting. Hence, they deduced that nanostructures could influence the PEC efficiency of semiconductor materials [91]. However, Beerman *et al*. reported that nanorods yielded higher PEC efficiencies than nanodendrites due to fewer grain boundaries which lead to fewer recombination sites [30].

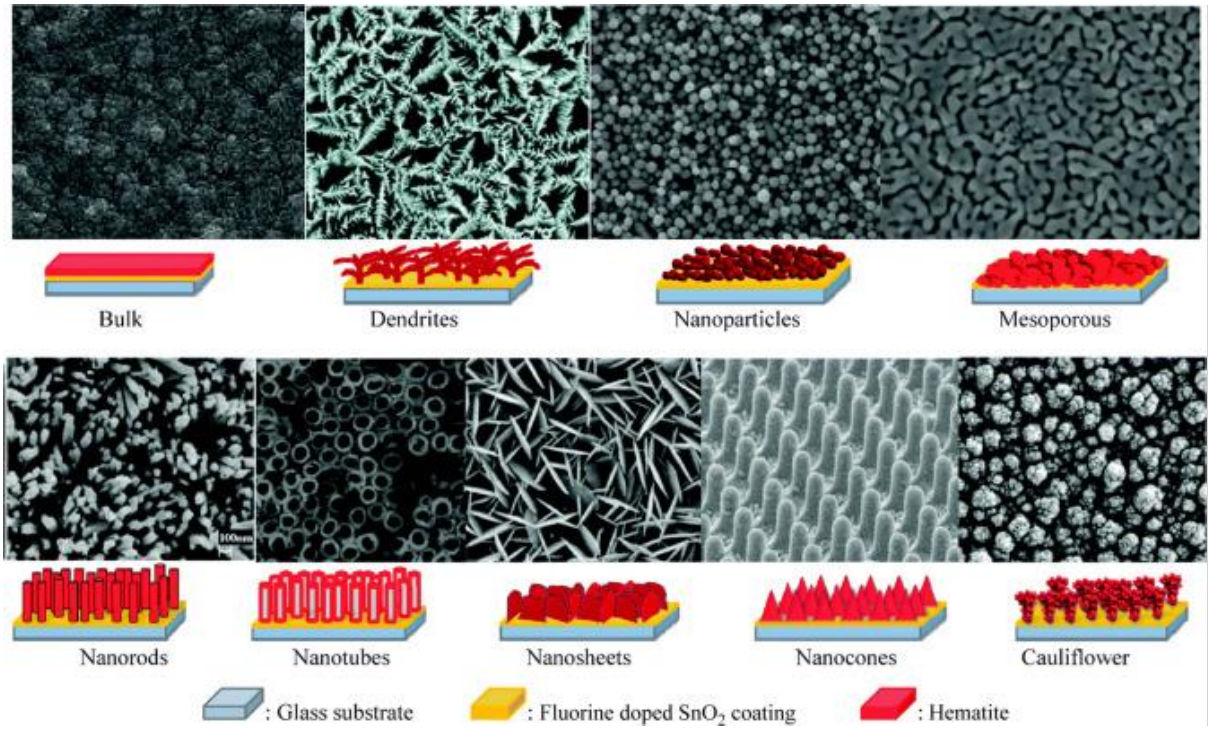

Figure 2.9.1. Illustration of bulk, dendrite, nanoparticle, mesoporous, nanorods, nanotubes, nanosheets, nanocones and cauliflower hematite nanostructuring [92].

2.10 Preparation techniques for hematite thin films

Recently, preparation techniques for hematite thin films have been used in comparative studies to optimize coating techniques. The synthesis of hematite depends on mixing methods, solution concentration, annealing time and temperature, concentrations of solutions and the rate of oxidation [93]. The particle morphology is influenced by aggregation, nucleation and adsorption of impurities along with the growth method [94]. Hence when choosing a suitable preparation technique, these factors need to be considered. Several techniques such as spin coating [95], spray-pyrolysis [96], dip coating [79], electrodeposition [96], electron beam lithography [97] and microemulsion precipitation [98] for preparing hematite thin films have been reported. In this dissertation, two colloidal solution-based techniques were used namely dip coating and spray-pyrolysis.

2.10.1 Dip coating

Dip coating is one of the most favoured colloidal solution-based preparation techniques due to the simplicity and cost efficiency of the method [99]. It is comprised of a beaker filled with a precursor solution and a dip coating unit. A cleaned substrate is slowly lowered into the precursor solution after which it is withdrawn at a constant rate which forms a thin coating on the substrate. Dip coating is known to form hematite nanoparticles [100] and nanospheres [101]. The nanoparticle sizing is dependent on the viscous drag, gravity, surface tension and inertial forces. Thus, various atmospheric disturbances could lead to surface defects such as dots and craters due to external particles landing on the wet substrate [95].

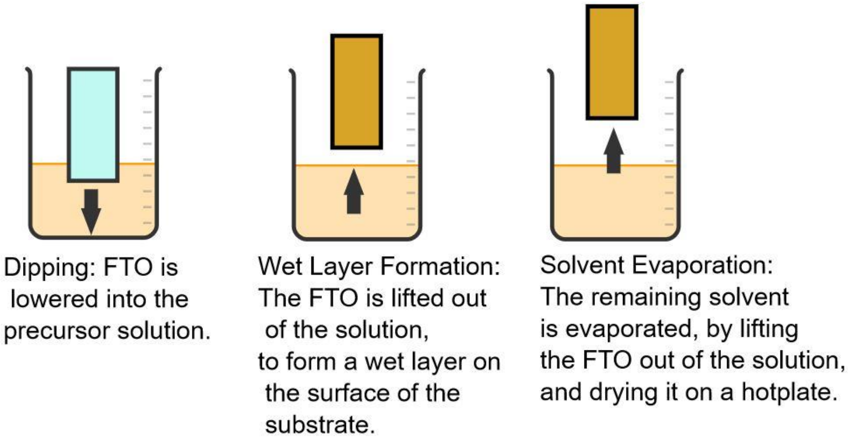

Figure 2.10.1. Schematic of dip coating preparation technique.

2.10.2 Chemical spray pyrolysis

Spray pyrolysis is another colloidal solution-based technique for preparing hematite thin films. Although it is not as cost efficient as dip coating, spray pyrolysis is favourable as it is simple, has deposition parameters that can be easily controlled and can cover a large surface area. This method involves a solution beaker, a substrate heater, an atomizer, and a temperature controller. The technique consists of an aqueous precursor solution which is sprayed onto a heated substrate (for the decomposition of the metallic compound): this forms a thin film coating on the substrate [102]. The fine mist droplets are transported from the atomizer to the nozzle and unto the substrate via a carrier gas such as pristine nitrogen or oxygen. Spray pyrolysis has the potential to produce a variation in nanoparticles such as nanospheres [103], nanocones [102] and nanorods [104].

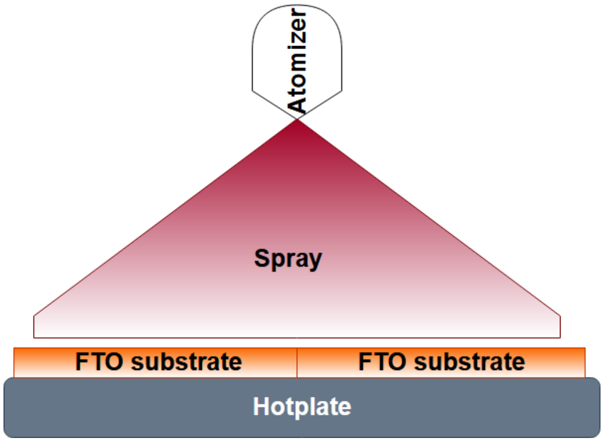

Figure 2.10.2. Schematic of spray pyrolysis coating technique.

2.10.3 Spin coating

Spin coating is a sol-gel based technique for hematite thin film production. Here, a few drops of the solution are placed onto the centre of a substrate. The substrate, placed in the spin coater is rotated at high fixed rotation speeds and subsequently forming a thin film on the substrate, which is then dried [105]. Spin coating produces a thin film of nanoparticles with a glossy appearance. This method is mostly used in combination with doping techniques [105]. The optical and structural properties of the thin film can be altered by the spin rate, precursor viscosity, turbulence, and the atmospheric humidity [95].

2.10.4 Electrodeposition

Electrodeposition is a favourable coating technique as it does not produce any waste, has a short fabrication time, can be done under low temperature and can be used to control particle size. However, electrodeposition is expensive due to the use of platinum counter and reference electrodes [106]. The crystallinity, composition, and nanoparticle size can all be controlled by varying the electron deposition parameters such as temperature, current density and electrolyte concentration. Meng *et al.* reported a working electrode of cleaned indium tin oxide glass (ITO), a counter electrode of iron plate and a reference electrode of calomel [107]. All three electrodes are placed in a single cell with an electrolyte of $FeCl_2$ and $FeCl_3$, as illustrated in figure 2.10.3 The iron plate was polished with emery paper and then degreased with acetone and ethanol and then rinsed with deionized water [107]. The films were rinsed with deionized water and left to dry in air. This method resulted in hematite nanoparticles forming on the surface of the ITO [107].

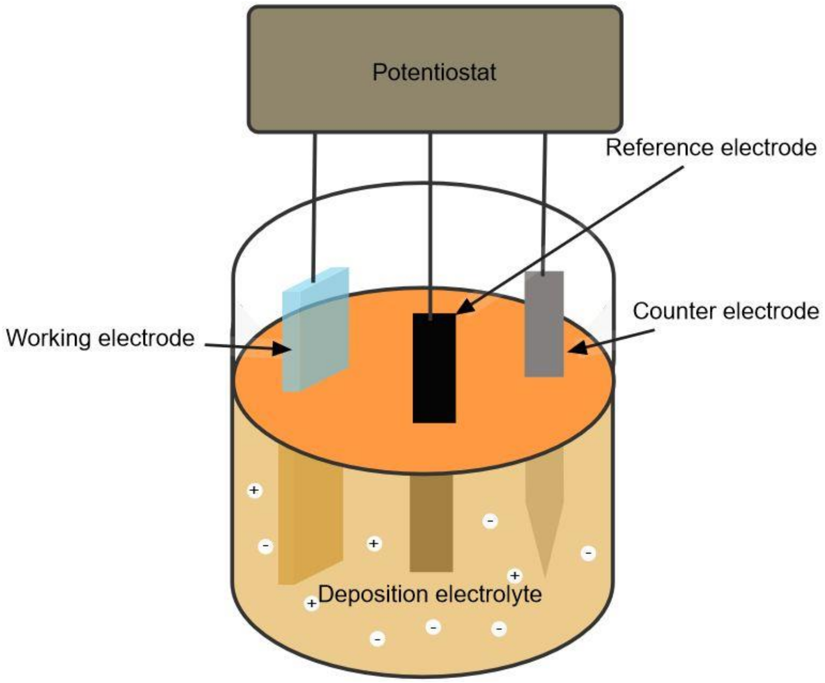

Figure 2.10.3. Schematic of the electrochemical deposition technique.

References

[1] Fujishima, A. and K. Honda, *Electrochemical photolysis of water at a semiconductor electrode.* nature, 1972. **238**(5358): p. 37-38.

[2] Fujishima, A. and K. Honda, *Electrochemical evidence for the mechanism of the primary stage of photosynthesis.* Bulletin of the chemical society of Japan, 1971. **44**(4): p. 1148-1150.

[3] Li, X., et al., *Engineering heterogeneous semiconductors for solar water splitting.* Journal of Materials Chemistry A, 2015. **3**(6): p. 2485-2534.

[4] Sivula, K., F. Le Formal, and M. Grätzel, *Solar water splitting: progress using hematite (α-Fe2O3) photoelectrodes.* ChemSusChem, 2011. **4**(4): p. 432-449.

[5] Qiu, J., et al., *Plasmon-enhanced water splitting on* TiO_2*-passivated GaP photocatalysts.* Physical Chemistry Chemical Physics, 2014. **16**(7): p. 3115-3121.

[6] Holmes, M.A., T.K. Townsend, and F.E. Osterloh, *Quantum confinement controlled photocatalytic water splitting by suspended CdSe nanocrystals.* Chemical communications, 2012. **48**(3): p. 371-373.

[7] Sathish, M., B. Viswanathan, and R. Viswanath, *Alternate synthetic strategy for the preparation of CdS nanoparticles and its exploitation for water splitting.* International Journal of Hydrogen Energy, 2006. **31**(7): p. 891-898.

[8] Wolcott, A., et al., *Photoelectrochemical study of nanostructured ZnO thin films for hydrogen generation from water splitting.* Advanced Functional Materials, 2009. **19**(12): p. 1849-1856.

[9] Ni, M., et al., *A review and recent developments in photocatalytic water-splitting using* TiO_2 *for hydrogen production.* Renewable and Sustainable Energy Reviews, 2007. **11**(3): p. 401-425.

[10] Yasuda, T., et al., *SiC photoelectrodes for a self-driven water-splitting cell.* Applied Physics Letters, 2012. **101**(5): p. 053902.

[11] Yu, X.-Y., et al., *High performance and reduced charge recombination of CdSe/CdS quantum dot-sensitized solar cells.* Journal of Materials Chemistry, 2012. **22**(24): p. 12058-12063.

[12] Yang, Y., et al., FeS_2*-anchored transition metal single atoms for highly efficient overall water splitting: a DFT computational screening study.* Journal of Materials Chemistry A, 2021. **9**(4): p. 2438-2447.

[13] Cabán-Acevedo, M., et al., *Ionization of high-density deep donor defect states explains the low photovoltage of iron pyrite single crystals.* Journal of the American Chemical Society, 2014. **136**(49): p. 17163-17179.

[14] Krysa, J., et al., TiO_2 *and* Fe_2O_3 *films for photoelectrochemical water splitting.* Molecules, 2015. **20**(1): p. 1046-1058.

[15] Pesci, F.M., et al., *Charge carrier dynamics on mesoporous* WO_3 *during water splitting.* The Journal of Physical Chemistry Letters, 2011. **2**(15): p. 1900-1903.

[16] Mallikarjuna, K., et al., *Synthesis of carbon-doped* SnO_2 *nanostructures for visible-light-driven photocatalytic hydrogen production from water splitting.* International Journal of Hydrogen Energy, 2020. **45**(57): p. 32789-32796.

[17] Gellé, A. and A. Moores, *Water splitting catalyzed by titanium dioxide decorated with plasmonic nanoparticles.* Pure and Applied Chemistry, 2017. **89**(12): p. 1817-1827.

[18] Kudo, A. and Y. Miseki, *Heterogeneous photocatalyst materials for water splitting.* Chemical Society Reviews, 2009. **38**(1): p. 253-278.

[19] Van de Krol, R. and M. Grätzel, *Photoelectrochemical hydrogen production*. Vol. 90. 2012: Springer.

[20] van de Krol, R., Y. Liang, and J. Schoonman, *Solar hydrogen production with nanostructured metal oxides.* Journal of Materials Chemistry, 2008. **18**(20): p. 2311-2320.

[21] Murphy, A., et al., *Efficiency of solar water splitting using semiconductor electrodes.* International journal of hydrogen energy, 2006. **31**(14): p. 1999-2017.

[22] Monfrecola, G., G. Moffa, and E. Procaccini, *Non-ionizing electromagnetic radiations, emitted by a cellular phone, modify cutaneous blood flow.* Dermatology, 2003. **207**(1): p. 10-14.

[23] Krishnakumar, R., et al., *Thin film preparation by spray pyrolysis for solar cells.* Materials chemistry and physics, 1987. **16**(5-6): p. 385-395.

[24] Ameri, T., et al., *Organic tandem solar cells: A review.* Energy & Environmental Science, 2009. **2**(4): p. 347-363.

[25] Malviya, K.D., et al., *Rigorous substrate cleaning process for reproducible thin film hematite (a-*Fe_2O_3*) photoanodes.* J. Mater. Res, 2015: p. 2.

[26] Rani, B.J., et al., *Design, fabrication, and characterization of hematite (α-*Fe_2O_3*) Nanostructures.* Jom, 2017. **69**(12): p. 2508-2514.

[27] Sivula, K., et al., *Photoelectrochemical water splitting with mesoporous hematite prepared by a solution-based colloidal approach.* Journal of the American Chemical Society, 2010. **132**(21): p. 7436-7444.

[28] He, Y., et al., *Size and structure effect on optical transitions of iron oxide nanocrystals.* Physical review B, 2005. **71**(12): p. 125411.

[29] Piccinin, S., *The band structure and optical absorption of hematite (α-*Fe_2O_3*): a first-principles GW-BSE study.* Physical Chemistry Chemical Physics, 2019. **21**(6): p. 2957-2967.

[30] Beermann, N., et al., *Photoelectrochemical studies of oriented nanorod thin films of hematite.* Journal of the Electrochemical Society, 2000. **147**(7): p. 2456.

[31] Kleiman-Shwarsctein, A., et al., *Electrodeposition of α-*Fe_2O_3 *doped with Mo or Cr as photoanodes for photocatalytic water splitting.* The Journal of Physical Chemistry C, 2008. **112**(40): p. 15900-15907.

[32] Debnath, N. and A. Anderson, *Optical spectra of ferrous and ferric oxides and the passive film: a molecular orbital study.* Journal of the Electrochemical Society, 1982. **129**(10): p. 2169.

[33] Badia-Bou, L., et al., *Water oxidation at hematite photoelectrodes with an iridium-based catalyst.* The Journal of Physical Chemistry C, 2013. **117**(8): p. 3826-3833.

[34] Ito, N.M., et al., *High temperature activation of hematite nanorods for sunlight driven water oxidation reaction.* Physical Chemistry Chemical Physics, 2017. **19**(36): p. 25025-25032.

[35] Hankin, A., J. Alexander, and G. Kelsall, *Constraints to the flat band potential of hematite photo-electrodes.* Physical Chemistry Chemical Physics, 2014. **16**(30): p. 16176-16186.

[36] Lee, J.B., et al., *Synthesis and magnetic properties of hematite particles in a "nanomedusa" morphology.* Journal of Nanomaterials, 2014. **2014**.

[37] Malviya, K.D., et al., *Rigorous substrate cleaning process for reproducible thin film hematite (α-Fe_2O_3) photoanodes.* Journal of Materials Research, 2016. **31**(11): p. 1565-1573.

[38] Kment, S., et al., *On the improvement of PEC activity of hematite thin films deposited by high-power pulsed magnetron sputtering method.* Applied Catalysis B: Environmental, 2015. **165**: p. 344-350.

[39] Kennedy, J.H. and K.W. Frese Jr, *Photooxidation of water at α-Fe_2O_3 electrodes.* Journal of the Electrochemical Society, 1978. **125**(5): p. 709.

[40] Misho, R. and W. Murad, *Band gap measurements in thin films of hematite Fe_2O_3, pyrite FeS_2 and troilite FeS prepared by chemical spray pyrolysis.* Solar Energy Materials and Solar Cells, 1992. **27**(4): p. 335-345.

[41] Hu, Y.-S., et al., *Improved photoelectrochemical performance of Ti-doped α-Fe_2O_3 thin films by surface modification with fluoride.* Chemical communications, 2009(19): p. 2652-2654.

[42] Bora, D.K., A. Braun, and E.C. Constable, *"In rust we trust". Hematite–the prospective inorganic backbone for artificial photosynthesis.* Energy & Environmental Science, 2013. **6**(2): p. 407-425.

[43] Dutta, A., et al., *Gap-plasmon enhanced water splitting with ultrathin hematite films: the role of plasmonic-based light trapping and hot electrons.* Faraday discussions, 2019. **214**: p. 283-295.

[44] Li, C., et al., *Surface, bulk, and interface: rational design of hematite architecture toward efficient photo-electrochemical water splitting.* Advanced Materials, 2018. **30**(30): p. 1707502.

[45] Shen, S., et al., *Hematite heterostructures for photoelectrochemical water splitting: rational materials design and charge carrier dynamics.* Energy & Environmental Science, 2016. **9**(9): p. 2744-2775.

[46] Le Formal, F., M. Grätzel, and K. Sivula, *Controlling photoactivity in ultrathin hematite films for solar water-splitting.* Advanced Functional Materials, 2010. **20**(7): p. 1099-1107.

[47] Paradzah, A.T., et al., *Use of interfacial layers to prolong hole lifetimes in hematite probed by ultrafast transient absorption spectroscopy.* Physica B: Condensed Matter, 2018. **535**: p. 138-142.

[48] Huang, X., et al., *N-Doped carbon dots: a metal-free co-catalyst on hematite nanorod arrays toward efficient photoelectrochemical water oxidation.* Inorganic Chemistry Frontiers, 2017. **4**(3): p. 537-540.

[49] Sun, Z., et al., *Enhanced photoelectrochemical performance of hematite photoanode by decorating NiCoP nanoparticles through a facile spin coating method.* Catalysis Letters, 2021: p. 1-10.

[50] Lo Vecchio, C., et al., *Enhanced photoelectrochemical water splitting at hematite photoanodes by effect of a NiFe-oxide co-catalyst.* Catalysts, 2020. **10**(5): p. 525.

[51] Xi, L., et al., *In situ XAS study of CoB i modified hematite photoanodes.* Dalton Transactions, 2017. **46**(45): p. 15719-15726.

[52] Neufeld, O., N. Yatom, and M. Caspary Toroker, *A first-principles study on the role of an Al_2O_3 overlayer on Fe_2O_3 for water splitting.* ACS Catalysis, 2015. **5**(12): p. 7237-7243.

[53] Deng, J., et al., *Thin-layer Fe_2TiO_5 on hematite for efficient solar water oxidation.* ACS nano, 2015. **9**(5): p. 5348-5356.

[54] Yan, K., et al., *Self-driven hematite-based photoelectrochemical water splitting cells with three-dimensional nanobowl heterojunction and high-photovoltage perovskite solar cells.* Materials today energy, 2017. **6**: p. 128-135.

[55] Paradzah, A.T., et al., *Photoelectrochemical performance and ultrafast dynamics of photogenerated electrons and holes in highly titanium-doped hematite.* Physical Chemistry Chemical Physics, 2020. **22**(46): p. 27450-27457.

[56] Pan, H., et al., *(Ti/Zr, N) codoped hematite for enhancing the photoelectrochemical activity of water splitting.* Physical Chemistry Chemical Physics, 2015. **17**(34): p. 22179-22186.

[57] Mirbagheri, N., et al., *Visible light driven photoelectrochemical water oxidation by Zn-and Ti-doped hematite nanostructures.* Acs Catalysis, 2014. **4**(6): p. 2006-2015.

[58] Phuan, Y.W., et al., *Prospects of electrochemically synthesized hematite photoanodes for photoelectrochemical water splitting: a review.* Journal of Photochemistry and Photobiology C: Photochemistry Reviews, 2017. **33**: p. 54-82.

[59] Bryan, J.D. and D.R. Gamelin, *Doped semiconductor nanocrystals: synthesis, characterization, physical properties, and applications.* Prog. Inorg. Chem, 2005. **54**(47): p. 47-126.

[60] Devi, L.G., B.N. Murthy, and S.G. Kumar, *Photocatalytic activity of TiO2 doped with* Zn^{2+} *and* V^{5+} *transition metal ions: Influence of crystallite size and dopant electronic configuration on photocatalytic activity.* Materials Science and Engineering: B, 2010. **166**(1): p. 1-6.

[61] Meng, X., et al., *Enhanced photoelectrochemical activity for Cu and Ti doped hematite: The first principles calculations.* Applied Physics Letters, 2011. **98**(11): p. 112104.

[62] Kumari, S., et al., *Characterization of Zn-doped hematite thin films for photoelectrochemical splitting of water.* Current science, 2006: p. 1062-1064.

[63] Li, M., et al., *Morphology and doping engineering of Sn-doped hematite nanowire photoanodes.* Nano letters, 2017. **17**(4): p. 2490-2495.

[64] Zhang, Y., et al., *Nonmetal P-doped hematite photoanode with enhanced electron mobility and high water oxidation activity.* Energy & Environmental Science, 2015. **8**(4): p. 1231-1236.

[65] Liao, P., J.A. Keith, and E.A. Carter, *Water oxidation on pure and doped hematite (0001) surfaces: Prediction of Co and Ni as effective dopants for electrocatalysis.* Journal of the American Chemical Society, 2012. **134**(32): p. 13296-13309.

[66] Anenburg, M., et al., *Iron cation vacancies in Pt (iv)-doped hematite.* Materials Advances, 2021.

[67] Nyarige, J.S., T.P. Krüger, and M. Diale, *Influence of precursor concentration and deposition temperature on the photoactivity of hematite electrodes for water splitting.* Materials Today Communications, 2020. **25**: p. 101459.

[68] Nyarige, J.S., T.P. Krüger, and M. Diale, *Effects of L-arginine concentration on hematite nanostructures synthesized by spray pyrolysis and chemical bath deposition.* Physica B: Condensed Matter, 2020. **581**: p. 411924.

[69] Simfukwe, J., et al., *Density Functional Theory study of Cu doped {0001} and {012} surfaces of hematite for water splitting.* MRS Advances, 2018. **3**(13): p. 669-678.

[70] Simfukwe, J., et al., *Exploring the stability and electronic properties of Zn-doped hematite surfaces for photoelectrochemical water splitting.* Journal of Physics and Chemistry of Solids, 2020. **136**: p. 109159.

[71] Liao, P., M.C. Toroker, and E.A. Carter, *Electron transport in pure and doped hematite.* Nano letters, 2011. **11**(4): p. 1775-1781.

[72] Simfukwe, J., et al., *Ab Initio Studies of Bimetallic-Doped {0001} Hematite Surface for Enhanced Photoelectrochemical Water Splitting.* Catalysts, 2021. **11**(8): p. 940.

[73] Wei, A., et al., *$Fe_2(MoO_4)_3$ modified hematite with oxygen vacancies for high-efficient water oxidation.* Chemical Engineering Journal, 2020. **395**: p. 125127.

[74] Tamirat, A.G., et al., *Photoelectrochemical water splitting at low applied potential using a NiOOH coated codoped (Sn, Zr) α-Fe_2O_3 photoanode.* Journal of Materials Chemistry A, 2015. **3**(11): p. 5949-5961.

[75] Bassi, P.S., et al., *Crystalline Fe_2O_3/Fe_2TiO_5 heterojunction nanorods with efficient charge separation and hole injection as photoanode for solar water oxidation.* Nano Energy, 2016. **22**: p. 310-318.

[76] Zhao, P., et al., *WO_3–α-Fe_2O_3 composite photoelectrodes with low onset potential for solar water oxidation.* Physical Chemistry Chemical Physics, 2014. **16**(4): p. 1327-1332.

[77] Hsu, Y.-K., Y.-C. Chen, and Y.-G. Lin, *Novel ZnO/Fe_2O_3 core–shell nanowires for photoelectrochemical water splitting.* ACS applied materials & interfaces, 2015. **7**(25): p. 14157-14162.

[78] Wang, M., et al., *Constructing Fe_2O_3/TiO_2 core–shell photoelectrodes for efficient photoelectrochemical water splitting.* Nanoscale, 2015. **7**(22): p. 10094-10100.

[79] Maabong, K., et al., *Nanostructured hematite thin films for photoelectrochemical water splitting.* Physica B: Condensed Matter, 2018. **535**: p. 67-71.

[80] Shen, S., et al., *Surface tuning for promoted charge transfer in hematite nanorod arrays as water-splitting photoanodes.* Nano Research, 2012. **5**(5): p. 327-336.

[81] Arzaee, N.A., et al., *Aerosol-assisted chemical vapour deposition of α-Fe_2O_3 nanoflowers for photoelectrochemical water splitting.* Ceramics International, 2019. **45**(14): p. 16797-16802.

[82] Chiam, S.Y., et al., *Improving the efficiency of hematite nanorods for photoelectrochemical water splitting by doping with manganese.* ACS applied materials & interfaces, 2014. **6**(8): p. 5852-5859.

[83] Chen, L., et al., *A comparative study of lithium-storage performances of hematite: Nanotubes vs. nanorods.* Journal of Power Sources, 2014. **245**: p. 429-435.

[84] Zhu, C., et al., *Plasma-induced oxygen vacancies in ultrathin hematite nanoflakes promoting photoelectrochemical water oxidation.* ACS applied materials & interfaces, 2015. **7**(40): p. 22355-22363.

[85] Lu, J., et al., *Hematite nanodiscs exposing (001) facets: synthesis, formation mechanism and application for Li-ion batteries.* Journal of Materials Chemistry A, 2013. **1**(17): p. 5232-5237.

[86] Liu, J., et al., *Ge-doped hematite nanosheets with tunable doping level, structure and improved photoelectrochemical performance.* Nano Energy, 2013. **2**(3): p. 328-336.

[87] Wang, L., et al., *Interface-engineered hematite nanocones as binder-free electrodes for high-performance lithium-ion batteries.* Journal of Materials Chemistry A, 2018. **6**(28): p. 13968-13974.

[88] Yu, B.Y. and S.-Y. Kwak, *Carbon quantum dots embedded with mesoporous hematite nanospheres as efficient visible light-active photocatalysts.* Journal of Materials Chemistry, 2012. **22**(17): p. 8345-8353.

[89] Tsege, E.L., et al., *Cu-doped flower-like hematite nanostructures for efficient water splitting applications.* Journal of Physics and Chemistry of Solids, 2016. **98**: p. 283-289.

[90] Zhang, Z., M.F. Hossain, and T. Takahashi, *Self-assembled hematite (α-*Fe_2O_3*) nanotube arrays for photoelectrocatalytic degradation of azo dye under simulated solar light irradiation.* Applied Catalysis B: Environmental, 2010. **95**(3-4): p. 423-429.

[91] Mao, A., et al., *Controlled synthesis of vertically aligned hematite on conducting substrate for photoelectrochemical cells: nanorods versus nanotubes.* ACS applied materials & interfaces, 2011. **3**(6): p. 1852-1858.

[92] Tamirat, A.G., et al., *Using hematite for photoelectrochemical water splitting: a review of current progress and challenges.* Nanoscale Horizons, 2016. **1**(4): p. 243-267.

[93] Domingo, C., R. Rodríguez-Clemente, and M. Blesa, *Morphological properties of α-FeOOH, γ-FeOOH and* Fe_3O_4 *obtained by oxidation of aqueous Fe (II) solutions.* Journal of colloid and interface science, 1994. **165**(1): p. 244-252.

[94] Baker, A.S., et al., *A structural study of haematite samples prepared from sulfated goethite precursors: the generation of axial mesoporous voids.* Journal of Materials Chemistry, 2000. **10**(3): p. 761-766.

[95] Kyesmen, P.I., N. Nombona, and M. Diale, *Influence of coating techniques on the optical and structural properties of hematite thin films.* Surfaces and Interfaces, 2019. **17**: p. 100384.

[96] Vanags, M., et al., *Comparison of the electrochemical properties of hematite thin films prepared by spray pyrolysis and electrodeposition.* Ceramics International, 2015. **41**(7): p. 9024-9029.

[97] Shin, S., et al., *A simple maskless process for the fabrication of vertically aligned high density hematite and graphene/magnetite nanowires.* Journal of Materials Chemistry C, 2017. **5**(6): p. 1313-1320.

[98] Garcia, A., et al., *Encapsulation of hematite in zircon by microemulsion and sol-gel methods.* Journal of sol-gel Science and Technology, 2003. **27**(3): p. 267-275.

[99] Gajda-Schrantz, K., et al., *Formation of an electron hole doped film in the α-*Fe_2O_3 *photoanode upon electrochemical oxidation.* Physical Chemistry Chemical Physics, 2013. **15**(5): p. 1443-1451.

[100] Hu, Q., et al., *Self-assembly of colloidal γ-Fe2O3 and FePt nanoparticles on carbon nanotubes by dip-coating process.* Journal of nanoscience and nanotechnology, 2012. **12**(2): p. 1709-1712.

[101] Zhang, J., et al., *Synthesis and gas sensing properties of α-*Fe_2O_3*@ZnO core–shell nanospindles.* Nanotechnology, 2011. **22**(18): p. 185501.

[102] Nyarige, J.S., T.P. Krüger, and M. Diale, *Structural and optical properties of hematite and L-arginine/hematite nanostructures prepared by thermal spray pyrolysis.* Surfaces and Interfaces, 2020. **18**: p. 100394.

[103] Cho, J.S., et al., *Design and synthesis of micron-sized spherical aggregates composed of hollow* Fe_2O_3 *nanospheres for use in lithium-ion batteries.* Nanoscale, 2015. **7**(18): p. 8361-8367.

[104] Hu, Z. and W. Li, *Preparation of superhydrophobic* Fe_2O_3 *nanorod films with the tunable water adhesion.* Journal of colloid and interface science, 2012. **376**(1): p. 245-249.

[105] Bellido-Aguilar, D.A., et al., *Effect of thermal treatment on solid–solid interface of hematite thin film synthesized by spin-coating deposition solution.* Thin Solid Films, 2016. **604**: p. 28-39.

[106] Fernandez, A. and R. Bhattacharya, *Electrodeposition of CuIn1− xGaxSe*$_2$ *precursor films: optimization of film composition and morphology*. Thin Solid Films, 2005. **474**(1-2): p. 10-13.

[107] Meng, Q., et al., *Fabrication of hematite (α-Fe*$_2$*O*$_3$*) nanoparticles using electrochemical deposition.* Applied Surface Science, 2016. **368**: p. 303-308.

3 Experimental

3.1 Introduction

In this chapter the fabrication of hematite nanoparticles using various coating techniques such as dip coating and spray pyrolysis will be discussed. Additionally, the synthesis of hematite nanoparticles using different annealing parameters are presented. Furthermore, the characterization techniques used in this study, namely X-ray diffraction, Raman spectroscopy, ultraviolet-visible spectroscopy, field emission scanning microscopy and electrochemical measurements are discussed.

3.2 Substrate cleaning

The substrate material used in this study was 1.5 cm x 3cm fluorine doped tin oxide (FTO) on glass. The substrates were degreased by rinsing with soapy water followed by deionized water. Furthermore, the substrates were soaked in a solution of sodium hydroxide for 10 minutes for etching. After which they were rinsed again with deionized water and sonicated with acetone, ethanol and isopropanol respectively, for 15 minutes each. Thereafter the FTO substrates were rinsed with deionized water and dried with pristine nitrogen (N_2) gas.

3.3 Synthesis of hematite nanoparticles via dip coating

Dip coating was used to deposit four layers of hematite onto the cleaned FTO substrates. A 2:1 mol ratio of iron(III)nitrate nonahydrate ($Fe(NO_3)_3.9H_2O$, Sigma Aldrich, AR, 99%) and oleic acid ($C_{18}H_{34}O_2$, Sigma Aldrich, GC, 99%) were mixed. The solution was heated at 110 °C for 2.5 hrs, forming a brick red mass of iron oleate ($C_{36}H_{66}FeO_4$). The iron oleate ($C_{36}H_{66}FeO_4$) solution obtained, was treated with tetrahydrofuran ($(CH_2)_4O$) and sonicated for 10 min. The solution was lastly centrifuged for 3 min at 5000 rpm. The supernatant solution was collected as a precursor solution for dip coating. The cleaned FTO substrates were dipped into the precursor solution and left for 2 min, after which, withdrawn at a 30 mm/min rate; then left to dry for 15 min on a hotplate at 70°C. Furthermore, the substrate was annealed at 500 °C for 1 hr, to form one layer of α-Fe_2O_3 crystals. The procedure was repeated four times and thus annealed four times in order to produce four layers of α-Fe_2O_3 thin film. Figure 3.3.1 presents the schematic setup for the dip coating technique.

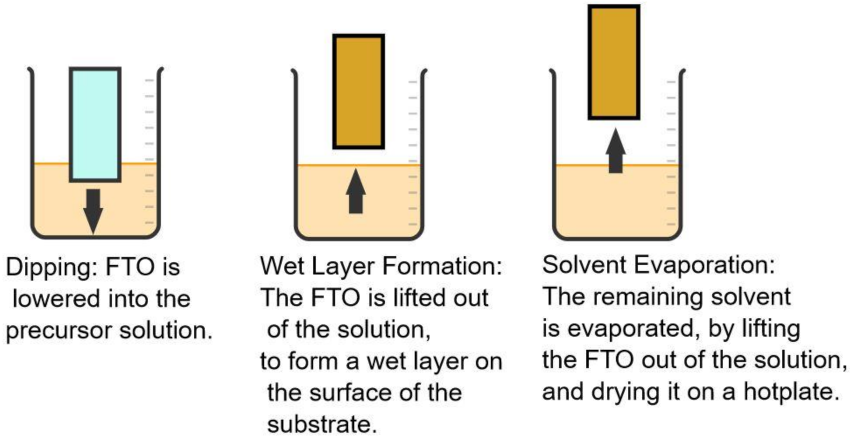

Figure 3.3.1. Schematic diagram of the dip coating technique used to synthesize hematite thin films.

3.4 Synthesis of hematite nanoparticles via spray pyrolysis

Chemical spray pyrolysis (CSP) was used to deposit thin layers of hematite on the FTO Substrates. The precursor solution was prepared by dissolving 50 mM of iron(III)nitrate nonahydrate ($Fe(NO_3)_3.9H_2O$, Sigma Aldrich, AR, 99%) into 200 ml of deionized water while stirring with a magnetic stirrer to form the precursor solution. The homogeneous supernatant solution was sprayed at a rate of 10 ml/min onto a heated FTO substrate, using pristine nitrogen (N_2) as a carrier gas. The FTO substrate was then heated to 400 °C using a hotplate, the nozzle diameter was set to 1 mm and 2 mm at a 20 cm height. The temperature was measured by a resistor thermocouple (Wavetek 23XT) while the flow rate was kept constant by a flow meter and spray time was kept at 30 s. After four layers of spray pyrolysis, the substrate was annealed once at 500 °C for 1 hr, forming four layers of α-Fe_2O_3 thin film. Figure 3.4.1 shows the schematic setup for spray pyrolysis.

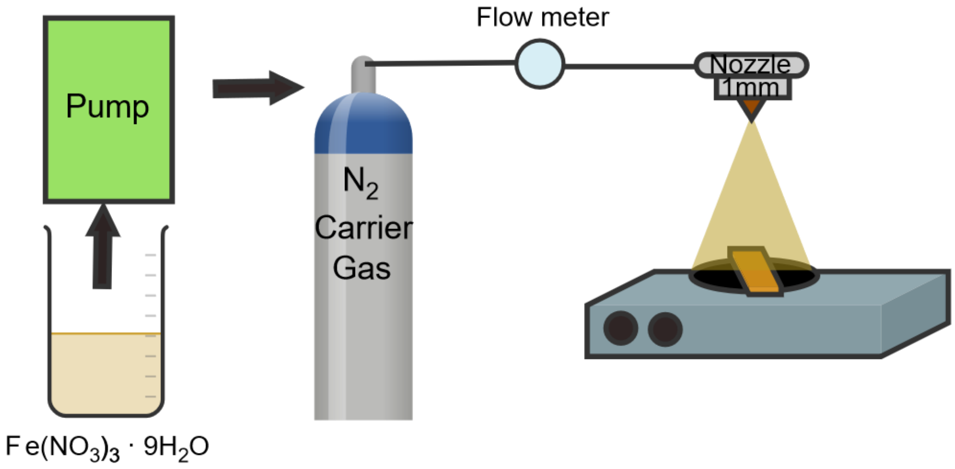

Figure 3.4.1. Schematic setup for the spray-pyrolysis technique used to prepare hematite thin films.

3.5 Synthesis of hematite nanoparticles with modified annealing

A control sample was prepared by CSP using 50 mM of $Fe(NO_3)_3.9H_2O$ to synthesize hematite nanoparticles. The nozzle diameter was set to 2 mm with a 30 s spray time at 20 cm height. Four layers were deposited after which the sample was annealed at 500 °C for 1 hr, to form a thin film. Similarly, a different sample was prepared with the same pre-set CSP parameters, however the annealing time was reduced to 500 °C for 30 mins. A third set of samples were prepared using the same pre-set CSP conditions, however one sample was prepared with only one layer of hematite annealed at 500 °C for 1 hr, whereas another sample was prepared with four layers of α-Fe_2O_3, annealed in between each layer, at 500 °C for 1 hr consecutively. All samples were then characterized.

3.6 Characterization of hematite nanostructures

3.6.1 X-ray diffraction

In 1912, X-ray diffraction was first discovered by von Laue for applications in solid state physics [1], recently this technique has been used for applications in electronics [2], geology [3], biology [4], material science [5], engineering [6] and environmental science [5]. X-ray diffraction is a non-destructive crystallography technique that makes use of Laue or Bragg diffraction to study the crystallinity of a sample. XRD provides more information on the crystallinity such as size, structure and orientation, it can also provide more detail on the microstrain, possible defects, lattice parameters and unit cell dimensions. The X-rays are generated by heating a PVP:TEC (polyvinylpyrrolidone) filament in a cathode tube which emits electrons. The electrons are accelerated towards a cobalt (Co), copper (Cu), molybdenum (Mo) or Chromium (Cr) target, this produces a monochromatic beam. The monochromatic beam is used to irradiate the sample crystals to produce scattering. The scattered rays undergo constructive interference within the crystal resulting in diffraction. The intensity of the X-rays is studied, as the detector and sample rotate, to provide information on the crystallography of the sample. In this study a Bruker D2 Phaser X-ray diffractometer with CuK_α radiation (1.5418 Å) was used (figure 3.6.2). This particular diffractometer makes use of constructive interference in the form of Bragg diffraction, the incident beam strikes the crystal surface with an angle of θ which is followed by a reflection of the same angle. Bragg’s equation denotes that $m\lambda = d\, sin\, \theta$, where m=1,2,3…, λ describes the wavelength, d describes the interlayer spacing and θ describes the incident angle. The diffraction peak relays information about the lattice spacing and unit cell metrics whereas the intensity describes the atom distribution [7]. Figure 3.6.1 provides a schematic overview of the inner workings of an X-ray diffractometer.

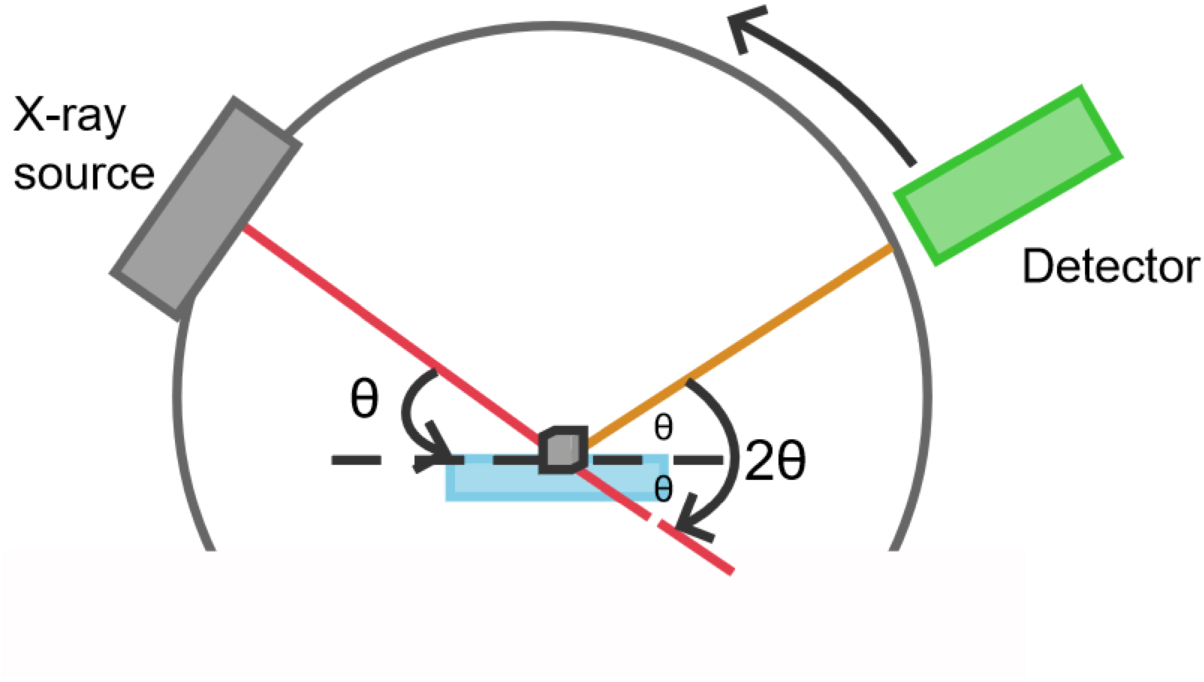

Figure 3.6.1. Illustration of the working components of an X-ray diffractometer.

To find the crystalline size, full width at half maximum measurements (FWHM) were calculated with the Origin Pro 9.1 software. The Debye-Scherrer formula was then used to estimate the crystalline sizes [8]:

$$D = \frac{k\lambda}{\beta \cos\theta} \tag{1}$$

Where D denotes the average crystal size, k denotes the shape factor, λ denotes the x-ray wavelength, β represents the FWHM and θ denotes the Bragg angle (in radians).

Figure 3.6.2. Photograph of the Bruker D2 Phaser X-ray diffractometer used in this study.

3.6.2 Raman spectroscopy

The inelastic scattering of photons or Raman scattering was first discovered by dr. C. V. Raman in 1928 [9]. Since then, Raman spectroscopy has been used in various fields such as pharmaceuticals [10], geology [11], material sciences [12] and cell biology [13]. Raman spectroscopy is a non-destructive technique that depends on the inelastic scattering of light interacting with molecular vibrations. Some of the photons undergo a frequency and wavelength change due to inelastic scattering, which relates to the vibrational energy of the sample material. The scattering can be one of three types, namely Rayleigh, stokes Raman or anti-stokes Raman scattering, where Rayleigh scattering implies that photons with unchanged energy, stokes scattering denotes photons that lost energy (larger wavelength) and anti-stokes scattering implies that photons have gained energy (shorter wavelength), as illustrated in figure 3.6.3. Thus, giving more information on the crystallinity, chemical structure, molecular interactions, polymorph and phase of a particular material. For Raman spectroscopy a monochromatic light is focused through the beam expander and the Rayleigh scattering is filtered out. The filtered light is then reflected to the microscope back onto the material, the scattered light is focused by a focussing mirror to the grating and lastly to the detector. In this study a WITec alpha300 RAS+ confocal Raman microscope was used with a green 532 nm excitation laser as shown in figure 3.6.5.

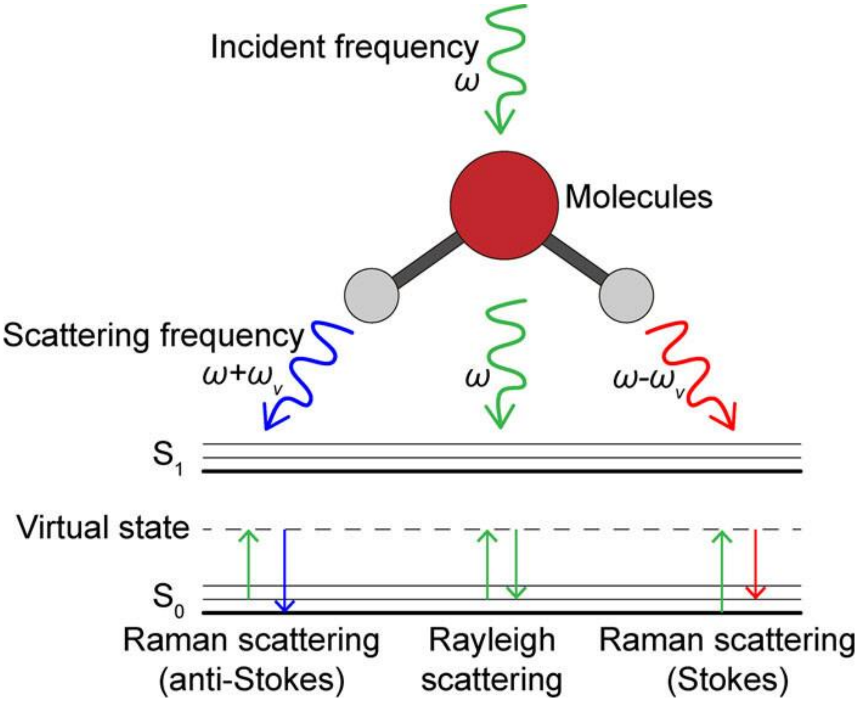

Figure 3.6.3. Schematic diagram of Raman anti-stokes, Raman stokes and Rayleigh scattering. [14]

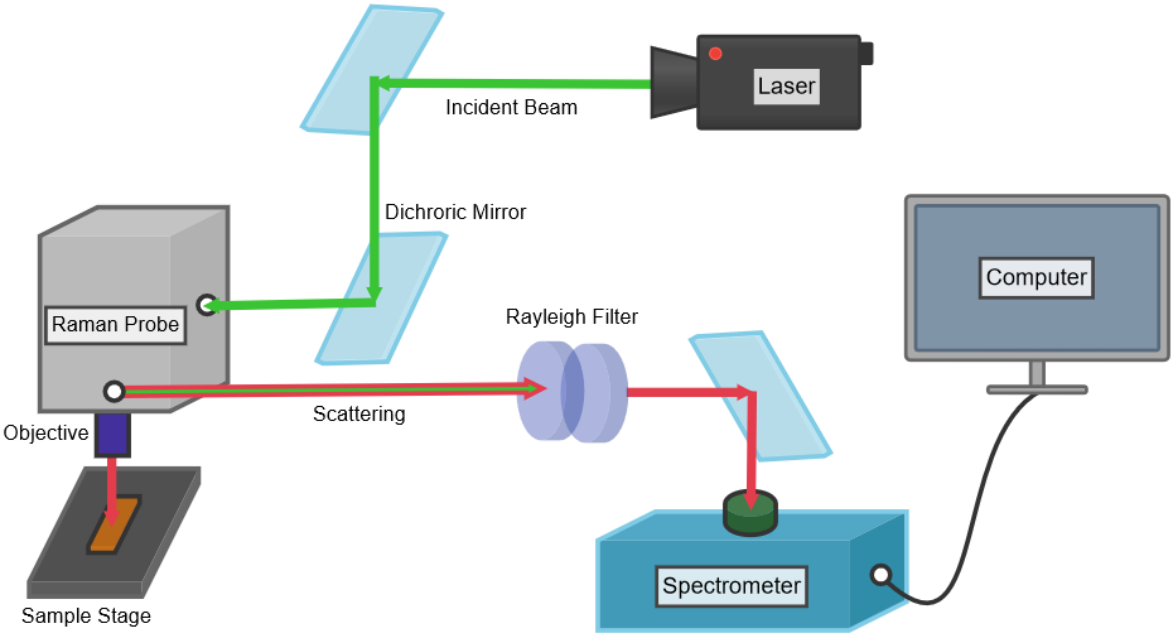

Figure 3.6.4. Diagram of the Raman spectroscopy setup.

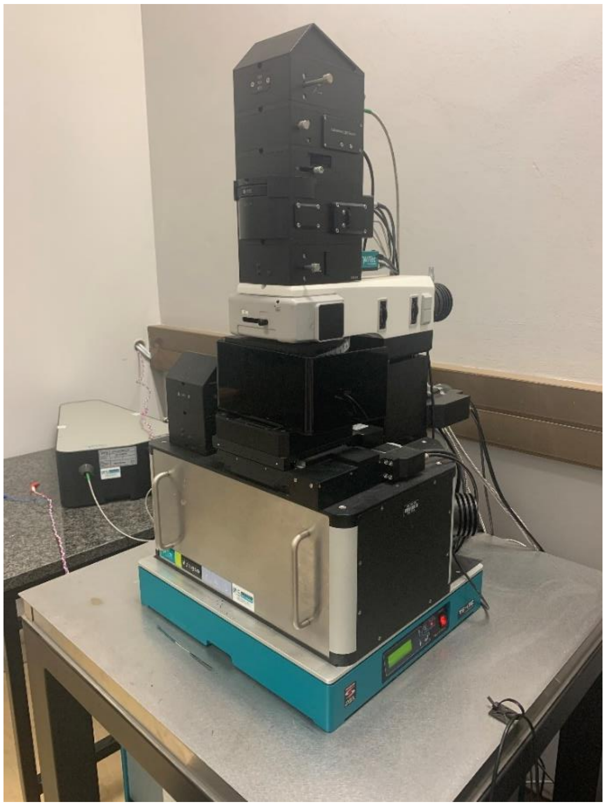

Figure 3.6.5. Photograph of the WITec alpha300 RAS+ Raman spectroscopy setup used in this study.

3.6.3 Scanning Electron Microscopy

Scanning electron microscopy (SEM) was first developed in 1937, by Manfred von Ardenne. SEM was based on the same principles as the electromagnetic lens which was first developed in 1926 by Hans Busch [15]. Field emission-SEM (FE-SEM) has since been heavily used to study the surface morphology and topography of various samples. FE-SEM is applicable in research fields ranging from material sciences (nanotechnology) [16], engineering [17], biology [18] to geology [19]. The FE-SEM consists of a tungsten filament electron gun, electron beam generation column, vacuum pump, lens, secondary electron detector, monitors and a control balance as illustrated in figure 3.6.6 [20]. Within the microscope, the materials' surface is scanned by a high energy electron beam, the electrons are focused through a magnetic lens on a small surface area, of nanometer scale, on the sample. As the electrons interact with the surface, they are either absorbed, reflected or excited to release secondary electrons such as backscattered electrons, Auger electrons or Bremssrahlung X-rays [21]. These secondary electrons are then detected by a secondary electron detector, the intensity of secondary electrons is highly dependent on the topography of the sample [22]. In this study a Zeiss Gemini Ultra Plus FEG-SEM and a Zeiss Gemini 2 Crossbeam 540 FEG SEM (operating at 1kV and 2kV) was used to study the surface morphology, along with the cross section of the hematite thin films. The samples had to be prepared by carbon coating, which increases conductivity and thus avoided surface charging, before they were loaded into the FE-SEM.

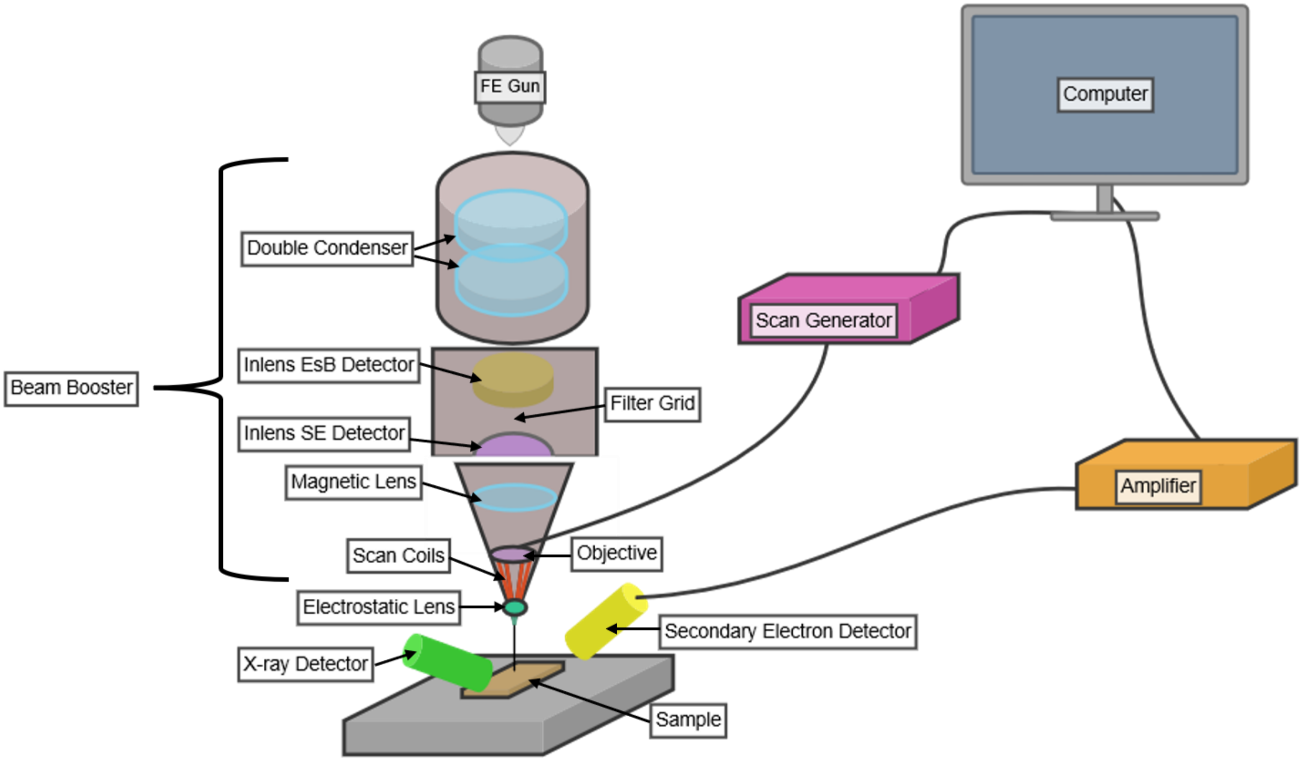

Figure 3.6.6. Illustration of a Zeiss Gemini 2 scanning electron microscope.

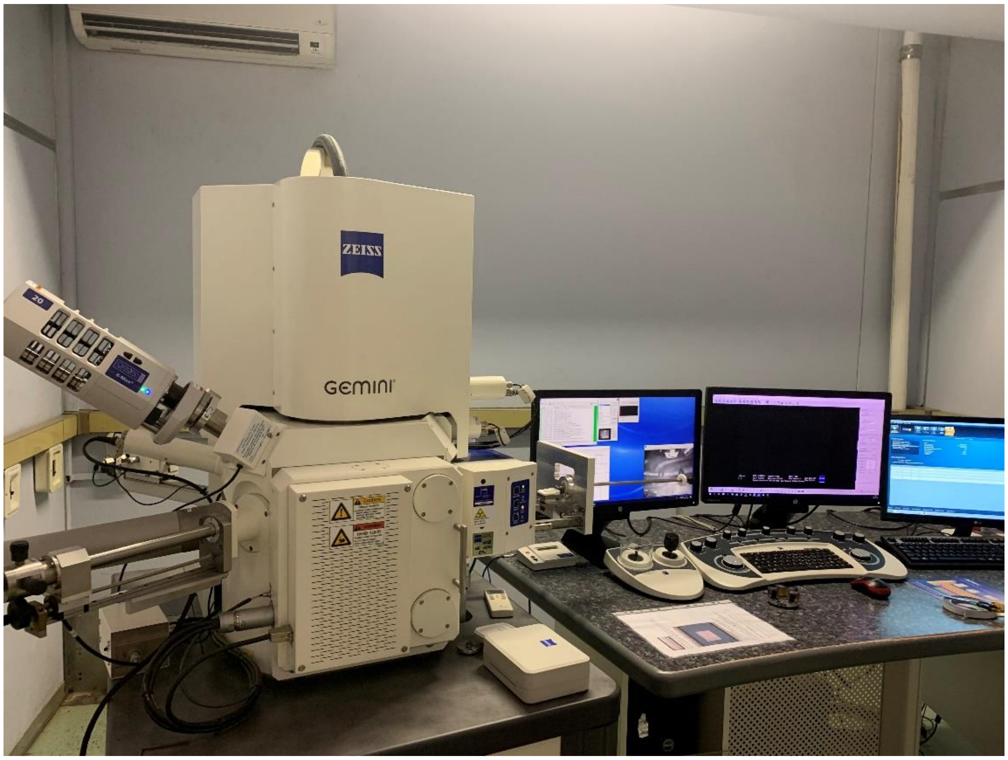

Figure 3.6.7. Photograph of a Zeiss Gemini 2 Crossbeam scanning electron microscope.

3.6.4 Ultraviolet-Visible (UV-VIS) spectroscopy

Ultraviolet-Visible (UV-Vis) spectroscopy was first developed by Arnold Beckman in 1935-1942, where it was used to determine the light absorption of vitamins [23] . UV-Vis is a non-destructive technique that measures the light absorption or transmittance of a material. The sample is illuminated by electromagnetic waves ranging from 200 – 400 nm (near ultraviolet) and 400 – 700 nm (visible) range. The sample interacts with the light and either reflects, absorbs or transmits the light, which is measured by the intensity before (I_0) and after (I) the sample. The absorbance and transmittance of the sample is described by the Beer-Lamberts equation [24]:

$$A = \varepsilon c l \tag{2}$$

$$\varepsilon cl = -\log\left(\frac{I}{Io}\right) = -\log(T) \quad (3)$$

$$A = -\log(T) \quad (4)$$

Where, A denotes the absorbance, ε denotes the absorption coefficient, c denotes the concentration, l denotes the path length of light through the sample and T denotes the transmittance. In this research a Cary 100 Bio UV-Vis spectrometer was used to measure the absorbance (figure 3.6.9). This spectrometer makes use of a blank substrate (FTO) along with the sample, both absorbances are measured and a baseline correction is done from the blank substrate (FTO). From these measurements, the bandgap was estimated using the onset absorption [25].

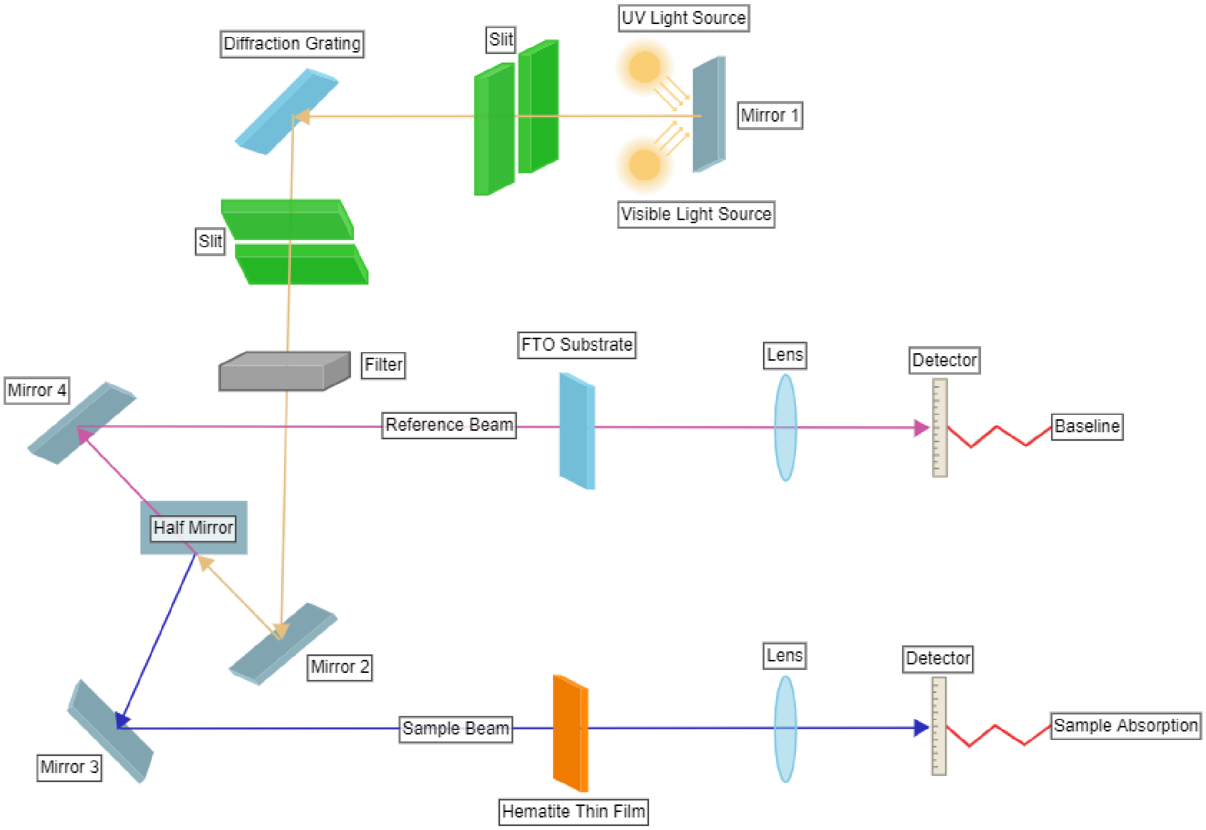

Figure 3.6.8. Schematic diagram of the UV-Vis spectrometer.

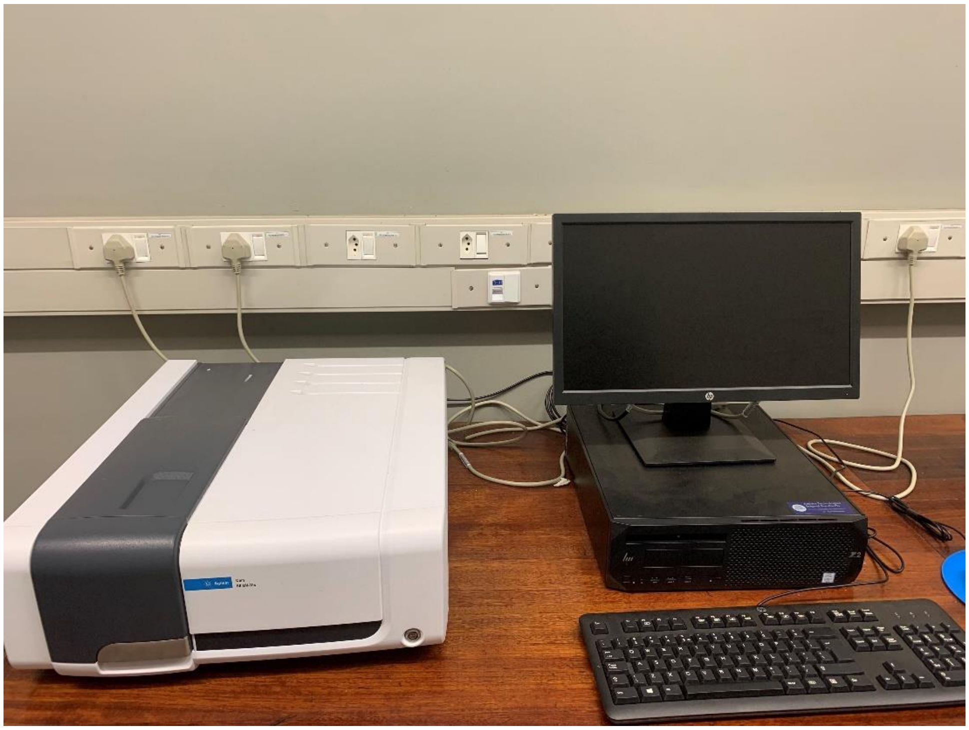

Figure 3.6.9. Photograph of the UV-Vis spectrometer used in this study.

3.6.5 Photoelectrochemical Measurements

The electrochemical properties of the hematite films were performed using a three electrode PEC cappuccino cell connected to a VersaSTAT 3F potentiostat as illustrated by figure 3.6.10. Two types of measurements namely Mott-Schottkey (M-S) and linear scan voltammetry (LSV) were performed. The three electrode PEC cappuccino cell consisted of an Ag/AgCl in 3M KCl reference electrode, a hematite thin film as the working electrode and platinum mesh as the counter electrode in a 1M NaOH, pH=13.6 electrolyte. Both dark and light measurements were performed at a scan rate of 50 mVs^{-1}. A Newport Oriel LSC 100 $mWcm^{-2}$ Xenon solar simulator (1 sun) was used to irradiate the 0.49 cm^2 hematite working electrode in the AM 1.5G spectrum. For the LSV measurements a voltage range of 0 to 1 was used. The current density equation was used to calculate the photocurrent produced when the simulated light intensity of 1 sun irradiated the working electrode with a known area:

$$J = \frac{I}{A} \tag{5}$$

Where, J denotes the current density, I denotes the current measurement and A denotes the working electrode area. The measured potentials were then converted to the RHE (reversible hydrogen electrode) scale using the Nernst equation [26]:

$$V_{RHE} = V_{(Ag/AgCl)} + 0.059pH + V^{0}_{(Ag/AgCl)} \tag{6}$$

Where, $V_{(Ag/AgCl)}$ denotes the measured potential versus the reference electrode $V^{0}_{(Ag/AgCl)} = 0.205$ V at 25°C. The pH value depends on the pH of the electrolyte which was NaOH for this study [27]. For the dark Mott-Schottky curves a potential ranging from -0.2 to 1V at a frequency of 10 000 Hz to 1 Hz was used.

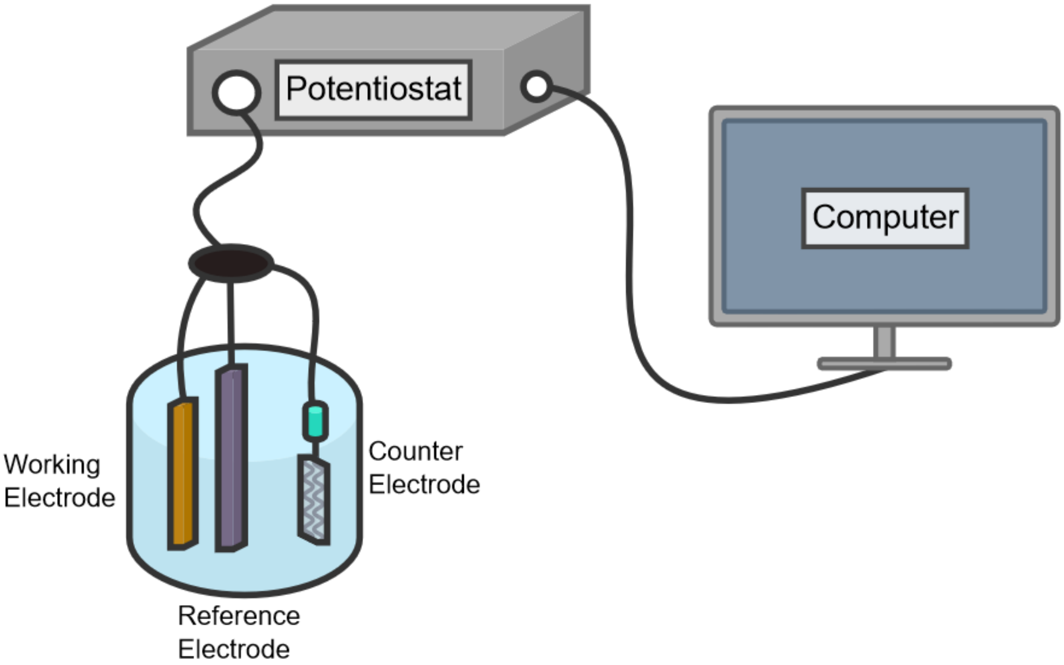

Figure 3.6.10. Schematic diagram of a three electrode PEC cappuccino cell with a 1 M NaOH electrolyte solution. The working electrode consisted of α-Fe_2O_3, the reference electrode consisted of Ag/AgCl and the counter electrode consisted of platinum mesh.

Figure 3.6.11. Photograph of the electrochemical setup including the VersaSTAT 3F potentiostat as used in this study.

References

[1] Eckert, M., *Max von Laue and the discovery of X-ray diffraction in 1912*. 2012, WILEY-VCH Verlag Berlin.

[2] Niu, G., et al., *Advanced Coherent X-Ray Diffraction and Electron Microscopy of Individual In P Nanocrystals on Si Nanotips for III-V-on-Si Electronics and Optoelectronics.* Physical Review Applied, 2019. **11**(6): p. 064046.

[3] Perrett, G.M., J.A. Maxwell, and J.L. Campbell, *Combined X-ray diffraction and alpha particle X-ray spectrometer analysis of geologic materials.* X-Ray Spectrometry, 2017. **46**(3): p. 171-179.

[4] Shi, Y., *A glimpse of structural biology through X-ray crystallography.* Cell, 2014. **159**(5): p. 995-1014.

[5] Tamura, N., et al., *Submicron x-ray diffraction and its applications to problems in materials and environmental science.* Review of scientific instruments, 2002. **73**(3): p. 1369-1372.

[6] Delhez, R., T.H. De Keijser, and E. Mittemeijer, *Role of x-ray diffraction analysis in surface engineering: Investigation of microstructure of nitrided iron and steels.* Surface Engineering, 1987. **3**(4): p. 331-342.

[7] Bunaciu, A.A., E.G. UdriŞTioiu, and H.Y. Aboul-Enein, *X-ray diffraction: instrumentation and applications.* Critical reviews in analytical chemistry, 2015. **45**(4): p. 289-299.

[8] Kyesmen, P.I., N. Nombona, and M. Diale, *Influence of coating techniques on the optical and structural properties of hematite thin films.* Surfaces and Interfaces, 2019. **17**: p. 100384.

[9] Raman, C.V., *A new radiation.* Indian Journal of physics, 1928. **2**: p. 387-398.

[10] Gordon, K.C. and C.M. McGoverin, *Raman mapping of pharmaceuticals.* International journal of pharmaceutics, 2011. **417**(1-2): p. 151-162.

[11] Henry, D.G., et al., *Raman spectroscopy as a tool to determine the thermal maturity of organic matter: Application to sedimentary, metamorphic and structural geology.* Earth-Science Reviews, 2019. **198**: p. 102936.

[12] Das, R.S. and Y. Agrawal, *Raman spectroscopy: recent advancements, techniques and applications.* Vibrational spectroscopy, 2011. **57**(2): p. 163-176.

[13] Matthäus, C., et al., *Infrared and Raman microscopy in cell biology.* Methods in cell biology, 2008. **89**: p. 275-308.

[14] Lin, L., et al., *Surface-enhanced Raman scattering nanotags for bioimaging.* Journal of Applied Physics, 2021. **129**(19): p. 191101.

[15] von Ardenne, M., *On the history of scanning electron microscopy, of the electron microprobe, and of early contributions to transmission electron microscopy.* The Beginnings of Electron Microscopy, 1985: p. 1-21.

[16] Zhou, W. and Z.L. Wang, *Scanning microscopy for nanotechnology: techniques and applications*. 2007: Springer science & business media.

[17] Moimas, L., et al., *Bioactive porous scaffolds for tissue engineering applications: Investigation on the degradation process by Raman spectroscopy and scanning electron microscopy.* Journal of Applied Biomaterials and Biomechanics, 2006. **4**(2): p. 102-109.

[18] Kessel, R.G. and C.Y. Shih, *Scanning Electron Microscopy in Biology: A Students' Atlas on Biological Organization*. 2012: Springer Science & Business Media.

[19] Reed, S.J.B., *Electron microprobe analysis and scanning electron microscopy in geology*. 2005: Cambridge university press.

[20] Egerton, R.F., *The scanning electron microscope*, in *Physical principles of electron microscopy*. 2005, Springer. p. 125-153.

[21] Kannan, M., *Scanning Electron Microscopy: Principle, Components and Applications.* A textbook on Fundamentals and Applications of Nanotechnology, 2018: p. 81-92.

[22] Kotera, M., T. Kishida, and H. Suga, *Monte Carlo simulation of secondary electrons in solids and its application for scanning electron microscopy.* Scanning Microscopy, 1990. **1990**(4): p. 8.

[23] GALLWAS, G., *ULTRAVIOLET SPECTROSCOPY*, in *Between Making And Knowing: Tools In The History Of Materials Research*. 2020, World Scientific. p. 457-473.

[24] Dhaliwal, A. and J. Hay, *The characterization of polyvinyl butyral by thermal analysis.* Thermochimica Acta, 2002. **391**(1-2): p. 245-255.

[25] Cao, R.-b., et al., *A facile route to synthesize nano-hematite colloid.* Materials Letters, 2011. **65(**21-22): p. 3298-3300.

[26] Tamirat, A.G., et al., *Sequentially surface modified hematite enables lower applied bias photoelectrochemical water splitting.* Physical Chemistry Chemical Physics, 2017. **19**(31): p. 20881-20890.

[27] Cho, E.S., M.J. Kang, and Y.S. Kang, *Enhanced photocurrent density of hematite thin films on FTO substrates: effect of post-annealing temperature.* Physical Chemistry Chemical Physics, 2015. **17**(24): p. 16145-16150.

4 Results and discussion

4.1 Introduction

In this chapter, the results obtained from the methods and computations as outlined in chapter 3 are presented. A three-part comparative study was performed, one discussing the influence of various colloidal-based coting techniques; two describing the optical, structural and electrical properties of α-Fe_2O_3 prepared with different annealing times and third the influence of layering and multiple annealing on the optical, structural and electrical properties of hematite nanoparticles.

4.2 Structural and optical properties of hematite nanostructures prepared by thermal spray pyrolysis and colloidal dip coating

Hematite thin films were prepared by two colloidal based techniques namely dip coating (DC) and spray pyrolysis (SP). Both thin films were prepared by layering four thin films of hematite and annealing once at 500 ºC.

Kyesmen *et al.* have reported on similar work on the influence of coating techniques of hematite thin films for photoelectrochemical (PEC) water splitting [1].

4.2.1 X-ray diffraction analysis

X-ray diffraction measurements of hematite that were done in the 2θ range of 20° and 80° as presented in figure 4.2.1. Seven peaks indicative of α-Hematite were identified: (012), (104), (110), (113), (024), (112) and (214). The six peaks were indexed at: 24.33º for (012), 33.94º for (104), 35.90º for (110), 49.81º for (024), 54.55º for (112) and 61.82º for (124) for the spray pyrolysis thin film and at: 24.35º for (012), 33.83º for (104), 35.73º for (110), 49.50 º for (024), 54.57º for (112) and 61.57º for (214) for the dip coated thin film. The peaks indicated with an asterix in figure 4.2.1 are indicative of the FTO-glass substrate. This correlates with the JCPDS 33-0664 plot card, which confirmed the crystalline structure hematite with the corundum structure [2, 3]. Similar diffraction peaks were obtained by Kyesmen *et al*. [14] when looking at the effects of coating techniques on the PEC behaviour of Hematite thin films.

The full width at half maximum is indicative of the size and state of the crystal structure. The narrow peaks indicate that the transformation of the crystal structure from ɣ- Fe_2O_3 (magnetite) to α-Fe_2O_3 (hematite) had taken place, when the samples were annealed at 500 °C [4, 5] (The calcination of iron-oxide takes place at temperatures above 400 °C). This confirmed the high purity of the α-Fe_2O_3 nanostructures. The diffraction patterns at (104) and (110) presents the rhombohedral structure of hematite denoted by the lattice constants of the trigonal-hexagonal unit cell a_{rh}=0.5427 nm and α=55.31° [3]. The more intense diffraction-peaks from the dip coating samples are indicative of a thicker film. Both methods produced peaks within a range of 0.10° of one another, indicating high similarity in crystal structure.

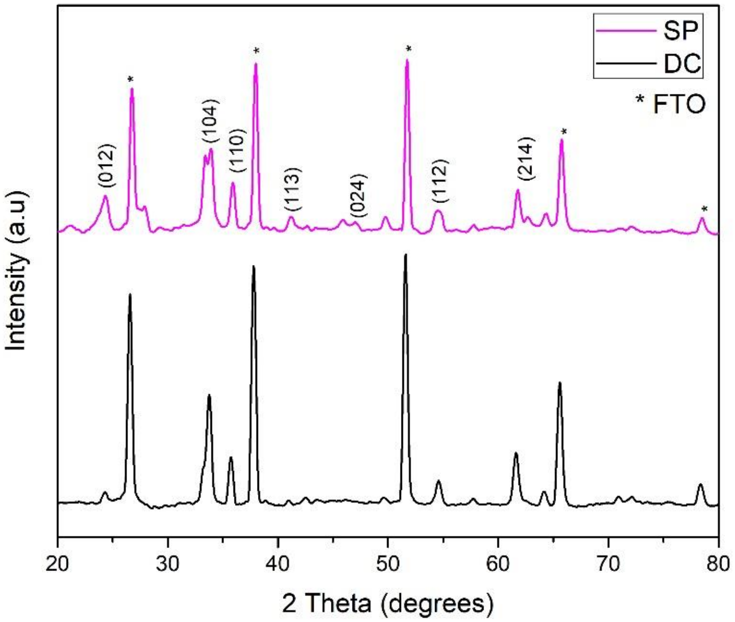

Figure 4.2.1. XRD patterns of α-Fe_2O_3 films synthesized by dip coating and chemical spray pyrolysis.

Full width at half maximum measurements (FWHM) were calculated with the Origin Pro 9.1 software using the six peaks for hematite. The Debye-Scherrer formula was then used to estimate the Crystallite sizes for each peak [6, 7]:

$$D = \frac{k\lambda}{d\cos\theta} \quad 4.2.1$$

Where D denotes the crystallite size, k denotes the shape factor (0.9), λ denotes the x-ray wavelength (0.15418 nm), d denotes the full width at half maximum in radians and θ denotes the diffraction angle in radians.

The average crystallite size for the dip coating thin film was computed as 11.5 nm whereas the average for spray pyrolysis was calculated as 15.45 nm. Thus, the crystallite sizing of the α-hematite thin films did vary when changing the coating technique. These crystallite sizes were similar when compared to those found in Nyarige *et al* [8].

Table 4.2.1. FWHM and crystal sizes of α-Fe_2O_3 nanoparticles prepared by dip coating

Peak	FWHM (Degrees)	2Theta (Degrees)	D Crystal-size (nm)	Peak
012	0,98	24,29	08,34	012
104	0,56	33,78	14,78	104
110	0,49	35,76	16,98	110
024	2,04	49,67	04,30	024
112	1,01	57,69	09,03	112
214	0,59	61,60	15,58	214

Table 4.2.2. FWHM and crystal sizes of α-Fe_2O_3 nanoparticles prepared by spray pyrolysis

Peak	FWHM (Degrees)	2Theta (Degrees)	D Crystal-size (nm)	Peak
012	0,97	24,34	08,37	012
104	0,42	33,93	19,81	104
110	0,53	35,91	15,71	110
024	0,62	49,77	14,08	024
112	0,46	51,75	19,42	112
214	0,60	61,80	15,34	214

4.2.2 Raman spectroscopy

Raman spectroscopy was performed, from which the crystallinity and structural information of the hematite thin films are presented in figure 4.2.2. Seven optical vibrational modes for hematite were found within the first Brillouin zone; two A_{1g} and five E_g modes confirmed with group theory [41, 42]. Both methods yielded polycrystal nanostructures presented by strong vibrational modes of A1g (230 cm^{-1}) and E_g (300 cm^{-1}) with high intensity which confirms the phase shift from magnetite to hematite has taken place. This substantiates the purity of the hematite thin films as already presented by XRD. The longitudinal optical (LO) mode was present at around 650 cm^{-1} and the two-phonon scattering modes, (2LO) at 1305 cm^{-1}. It was found that the 2LO mode had double the wavenumber of the LO mode, which confirms the ferromagnetic properties of hematite. If this phenomenon does not occur, then an impurity of magnetite could be assumed. There was a red shift in the sample prepared by dip coating as opposed to the one prepared by spray-pyrolysis, indicated by broadening of the E_g peaks, as a result of phonon-phonon scattering. The difference in intensity of peaks could be attributed to the frequency of annealing. The dip coating samples had been annealed four times between each layer, as opposed to the spray-pyrolysis sample which had been annealed once. The higher peak intensities of the E_g modes could be indicative of improved crystallinity. This confirms the results obtained by XRD.

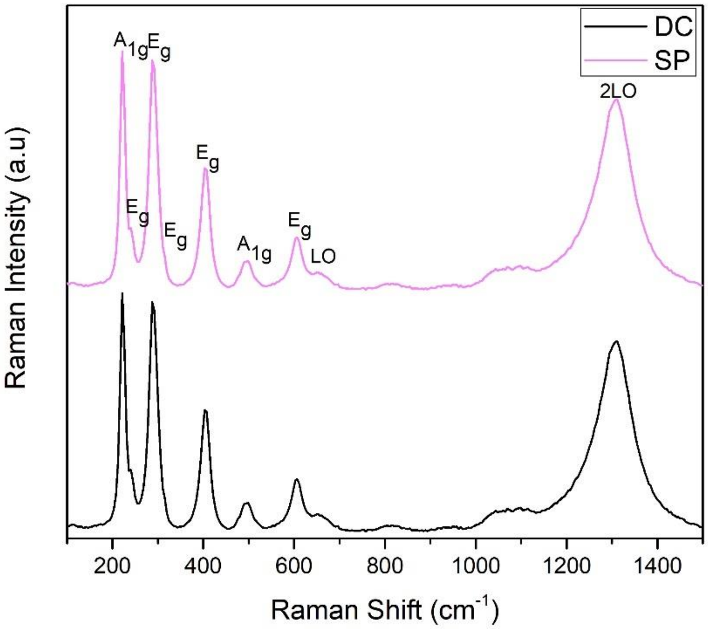

Figure 4.2.2. Raman spectroscopy of α-Fe_2O_3 films prepared by dip coating and spray pyrolysis coating techniques annealed at 500 °C.

4.2.3 Surface morphology

The surface morphology of the nanoparticles was observed by field emission-scanning microscopy (FE-SEM). From figure 4.2.3, it is evident that both samples contained homogenous nanoparticles. From figure 4.2.3 b and d it could be concluded that the dip coating nanoparticles had a uniform spherical appearance, whereas the spray-pyrolysis particles presented the agglomeration of various shapes, including nanospheres, nanolarvae and nanodisks. The nanostructuring into spherical nanoparticles has been reported to improve photocurrent production. From figures 4.2.3 a and c it appeared that the spray-pyrolysis film presented a more homogeneous morphology than the dip coating thin film. This was attributed to the even distribution during spraying when deposited, as well as the viscous drag of the dip coating solution. The grain size of the spray pyrolysis nanostructures was found to be smaller than those of the dip coating. Small homogeneous particles are favourable in PEC water splitting. The physical appearance of the films presented as an orange-brown colour, indicative of the absorption wavelength. It has been reported that the orange-brown colour causes hematite to absorb up to 40 % of visible light. The grain size was determined with Average Grain Intercept (AGI) as 45.82 nm for the spray pyrolysis thin film as opposed to 50 nm for the dip coated thin film.

Figure 4.2.3. FE-SEM images of α-Fe_2O_3 nanoparticles prepared by (a,b) chemical spray pyrolysis and (c,d) dip coating.

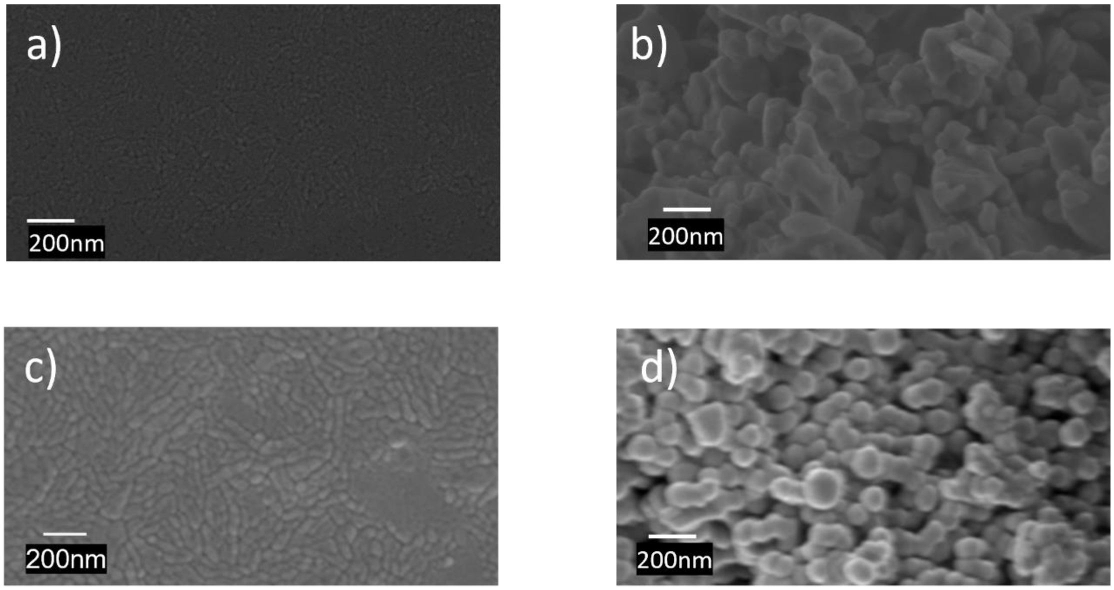

4.2.4 Optical studies

Optical studies were performed on the hematite thin films using UV-Vis spectroscopy shown in figure 4.2.4. The absorbance of the sample prepared by spray pyrolysis was significantly more than those prepared by the dip coating technique. Both samples showed wavelength values of above 500 nm which indicated good absorption for hematite. Both samples showed similar absorption in the visible spectra, with maximum peaks of 442.21 nm and 448.43 nm respectively for dip coating and spray pyrolysis. The lower absorbance of the dip coated film could partially be attributed to the smoother and glossier surface appearance of the dip coated film, which could possibly lead to surface reflection. The bandgap of both samples was estimated by Planck's Law:

$$E_g = \frac{hc}{\lambda} \tag{4.2.2}$$

, where Eg is the energy bandgap, c is the speed of light, v is the frequency of the proton (given by c = v λ) and λ is the wavelength. These wavelengths were similar when compared to those found in Nyarige *et al.* using a Tauc plot [31, 40].

The wavelength, as indicated by an arrow, was 596.75 nm for the DC film which led to an estimated bandgap of 2.08 eV whereas SP presented a wavelength of 608.57 nm, which led to a smaller estimated bandgap of 2.03 eV. It could thus be deduced that the spray pyrolysis film was favourable due to its small nanoparticle size, high purity and small bandgap, which could indicate higher electron flow.

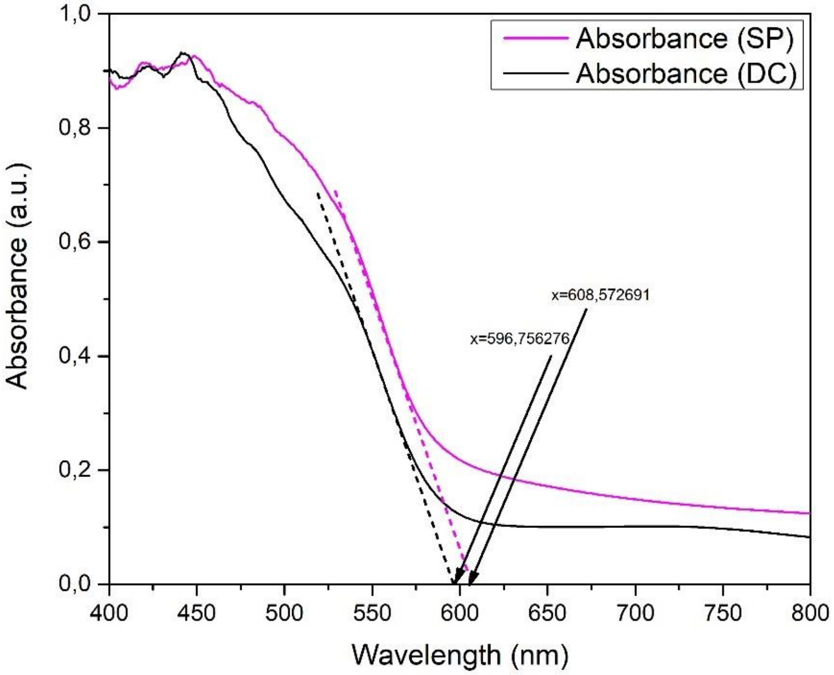

Figure 4.2.4. Absorbance spectra of α-Fe_2O_3 films prepared by dip coating and spray pyrolysis coating techniques.

4.3 Influence of annealing time on the structural and optical properties of hematite

Annealing time has been reported to influence the optical, structural, and electrical properties of the hematite nanoparticles. In this section two samples were prepared at a variation of 30 mins and 1 hr. Both samples were prepared by chemical spray pyrolysis.

Similar studies have been performed by Nyarige *et al.* on the influence of deposition temperature on the photoactivity of α-Fe_2O thin films [9].

4.3.1 X-ray diffraction analysis

Figure 4.3.1 presents the XRD measurements of the thin film hematite in the 2θ range of 20 ° and 80 °. Seven peaks correlating to the JCPDS 33-0664 plot card with the corundum structure [2, 3] were found: (012), (104), (110), (024), (122) and (124). The rhombohedral structure of α-Fe_2O can be seen by the (104) and (110) diffraction patterns as denoted by the $a=b=0.5034$ nm and $c=1.375$ nm lattice constants of the hexagonal unit cell [3]. These eight peaks were indexed at: 24.28º for (012), 33.95º for (104), 35.83º for (110), 41.04º for (024), 49.70º for (024), 54.61º for (112) and 61.70º for (124). For both samples the peaks were in a 2.5º range of one another which indicates similarity in structure. Nyarige *et al.* reported similar results when looking at the influence of precursor concentration for pristine Hematite [13].

The peak width was slightly increased for the sample that was annealed for 1 hr which indicates a decrease in overall crystalline size. Both graphs presented narrow peaks which indicate that the phase change to α-Fe_2O from magnetite has taken place during annealing [4, 5]. This confirmed the high purity of the hematite thin films. However, the film that was annealed for 30 mins presented more intense peaks which could be due to surface texture or crystal arrangement [10]. The nanoparticles annealed for 1 hr showed slightly smaller average crystallite grain size of 12.92 nm as compared to the film annealed for 30 mins which presented an average crystallite size of 13.35 nm. Smaller crystallite size could potentially be favourable as it increases the absorption area.

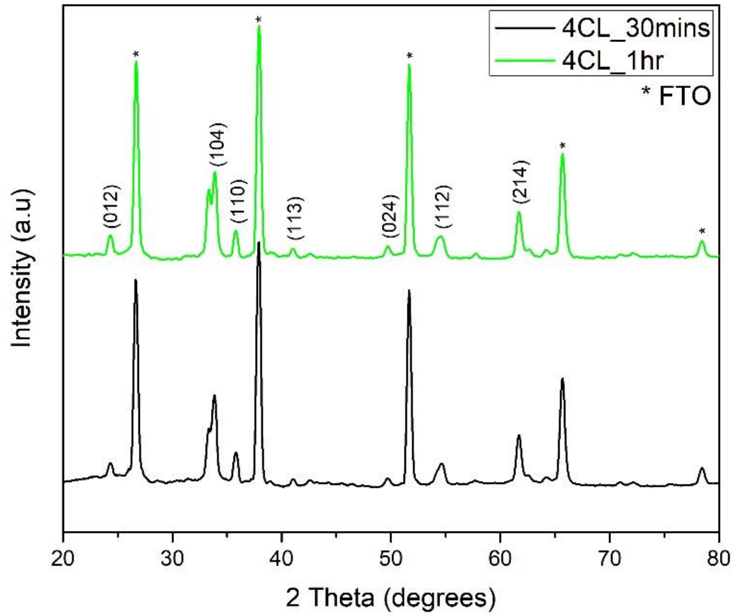

Figure 4.3.1. XRD patterns of α-Fe_2O_3 films synthesized by variating the annealing time from 30 minutes to 1 hour annealed at 500 ºC.

Table 4.3.1. FWHM and crystallite sizes for the (110) and (104) miller indices for both hematite films prepared at 30 mins and 1 hr annealing.

Sample	Peak	FWHM (°)	2 Theta (°)	Crystal size (nm)
30 minutes	(104)	0.88	33.73	10.83
30 minutes	(110)	0.62	35.80	15.86
1 hour	(104)	1.23	33.68	7.78
1 hour	(110)	0.54	35.80	18.05

4.3.2 Raman spectroscopy

Structural information regarding the crystallinity of the hematite thin films were determined by Raman spectroscopy as presented in figure 4.3.2. The polycrystallinity of both films were confirmed by the narrow intense vibrational modes. Two $_{A1g}$ vibrational modes were found at 230 cm^{-1} and 501 cm^{-1} whereas four E_g modes were found at 250 cm^{-1}, 300 cm^{-1}, 415 cm^{-1} and 615 cm^{-1} respectively which correlates to the values obtained by Kyesmen *et al.* in 2019 and Nyarige *et al.* in 2020 [1, 8]. The 2LO and LO modes were observed at 1325 cm^{-1} and 663 cm^{-1} respectively. From literature, Lopez *et al.* [16] noted that the 2LO and LO modes describe the magnetic properties of hematite with the 2LO mode having double the wavenumber of the LO mode, however due to the magnon scattering mode, there was a slight blue shift in the 2LO mode. The peak intensity seemed to decrease with annealing time, this could be attributed to crystallinity size which directly impacts the Raman intensity.

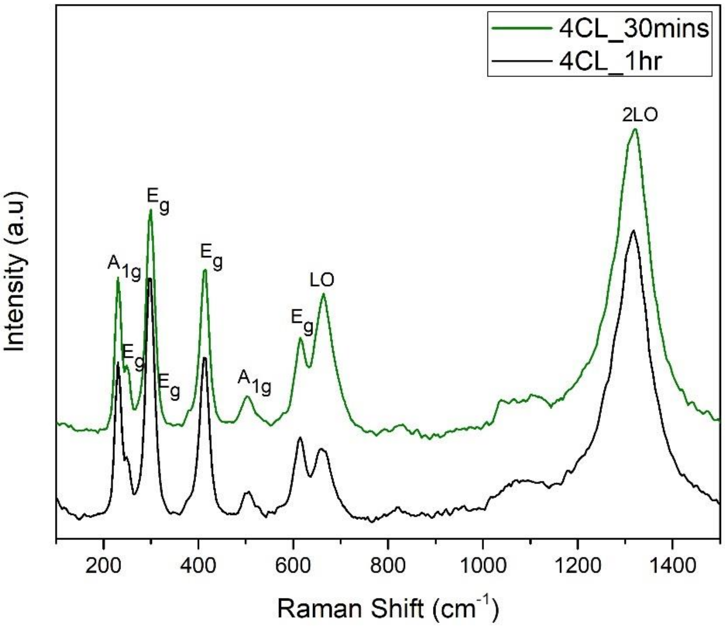

Figure 4.3.2. Raman spectroscopy of hematite films prepared at 30 mins and 1 hr of annealing.

4.3.3 Cross-sectional analysis

The thickness of the nanostructured films was measured by taking a cross-section of the film under field emission-scanning microscopy. The width of the thin films was obtained by excluding the thickness of the FTO substrates. The thickness was shown to increase from 669.9 nm to 870.3 nm with longer annealing time as shown in figure 4.3.3 This could be attributed to the full crystallization from magnetite to hematite at longer annealing times.

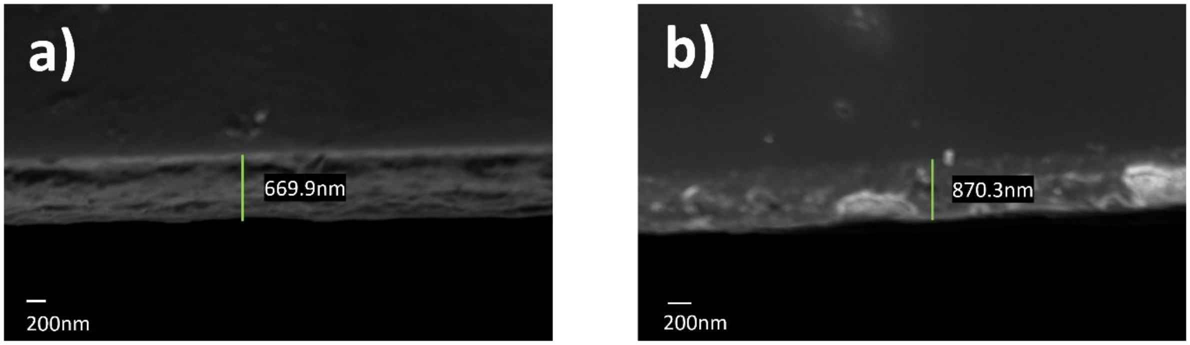

Figure 4.3.3. Cross-sectional micrograph images estimating the thickness using FE-SEM for four hematite films annealed at (a) 30 mins and (b) 1 hr.

4.3.4 Surface morphology

The surface morphology and topography of the nanoparticles were observed at different annealing times. The particle size was determined by AGI using the Image J software. A decrease in particle size from 50.40 nm to 33.23 nm was observed with increased annealing time. The change in particle size could be attributed to a change in crystallinity ranging from amorphous to agglomerated nanospheres as shown in figure 4.3.4. Small grain size could be beneficial as it leads to a decrease in grain boundaries which reduces the distance which charge carriers need to travel to reach the surface of the semiconductor. This led to increased electrochemical performance due to less recombination. Similar grain sizes have been reported by Kyesmen *et al.* on the effects of film thickness and coating techniques. They reported nanostructures with an average size of 29.55 +/- 5.7 nm.

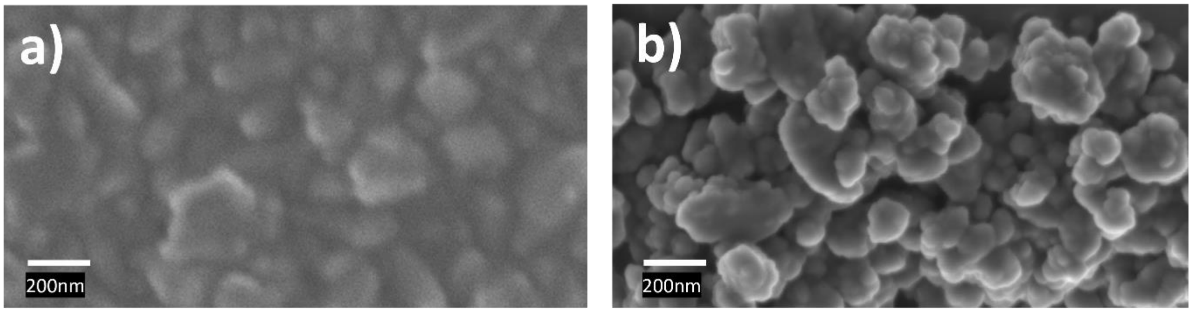

Figure 4.3.4. FE-SEM images of α-Fe_2O_3 nanoparticles prepared by (a,b) dip coating and (c,d) spray-pyrolysis.

4.3.5 Optical studies

Optical studies performed on the hematite thin films using a UV-Vis spectrometer in the range 400 – 800 nm are presented in figure 4.3.5. The film that was annealed for 30 mins yielded slightly better results than that of the film annealed at 1 hr. A red shift was observed with an increase of annealing time. The absorbance presented a linear relation in the red solar spectra, this is indicative that the d-d transition has taken place. The onset absorbance was found ranging between 615.86 to 624.31 nm as the annealing time increased from 30 mins to 1 hr. Furthermore, it can be concluded that there is high absorption in the visible region for both films.

The bandgaps of both films were estimated using the phonon equation given by:

$$E_g = \frac{hc}{\lambda} \qquad 4.3.1$$

Where Eg denotes the bandgap in eV, h denotes Planck's constant, c denotes the speed of light and λ denotes the wavelength. The bandgaps were estimated at 2.01 eV and 1.99 eV for the 30 mins and 1 hr α-Fe_2O_3 films. Similar bandgaps have been reported by Maabong *et al.* in the range 1.9-2.3 eV for hematite nanoparticles [11].

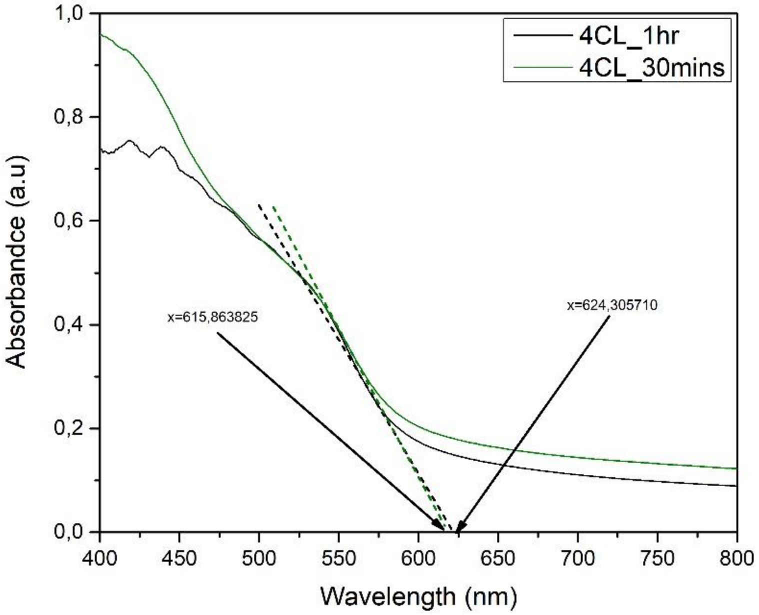

Figure 4.3.5. Absorbance spectra of α-Fe_2O_3 films prepared by annealing for 30 mins and 1 hr.

4.3.6 Mott-Schottky analysis

Mott-Schottky (M-S) analysis were performed under dark conditions on both the thin film annealed for 30 mins and the film annealed for 1 hr. This was done to study the electronic properties of the films using 1/capacitance against potential graphs as depicted in figure 4.3.6. The potential measurements were done at a 10 kHZ frequency. All M-S slopes were observed as positive which is indicative of n-type semiconductor properties. The values for the carrier density (N_D) and flat band potential (V_{FB}) were estimated using the M-S equation [12]:

$$\frac{1}{C^2} = \left(\frac{2}{\varepsilon_0 \varepsilon e N_D}\right)\left(V - V_{FB} - \frac{K_B T}{e}\right) \qquad 4.4.3$$

, where C denotes the capacitance of the space charge, ε_0 denotes the dielectric permittivity of a vacuum, ε denotes the dielectric constant which is given as 80 for α-Fe_2O_3, e denotes the charge of an electron, N_D denotes the donor density, V denotes the applied potential of the reference electrode, V_{FB} denotes the flat band potential, k denotes the Boltzmann constant and T denotes the temperature.

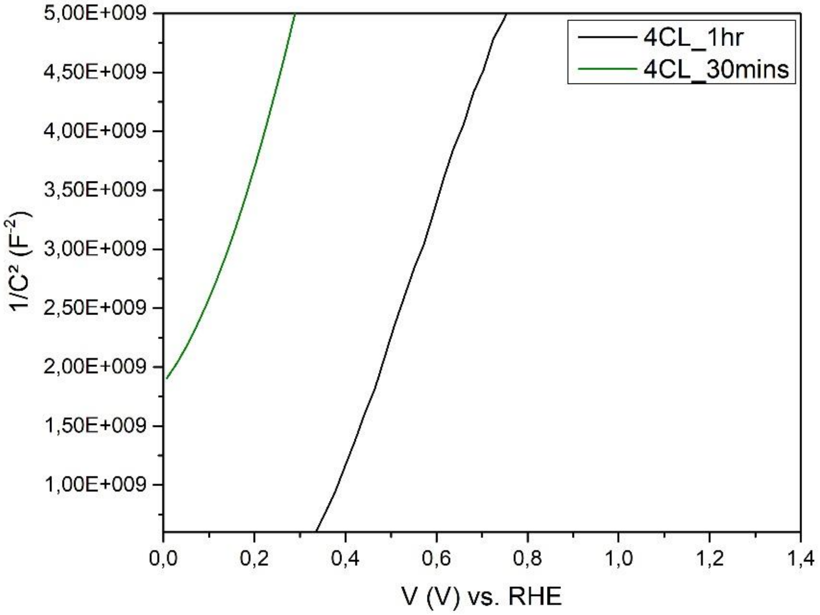

Figure 4.3.6. Mott-Schottky analysis plots of hematite thin films prepared by annealing for 30 mins and 1 hr.

From figure 4.3.6 the slopes were calculated using a linear fit to acquire the carrier density (N_D), whereas the x-intercept of the straight line was determined with extrapolation to estimate the flat band potential (V_{FB}). Both films had a donor density in the range of 10^{18} cm^{-3}. The α-Fe_2O_3 film prepared by 30 mins annealing showed a slightly smaller flat band potential 0.111 V and a much lower donor density of 2.30x10^{18} cm^{-3} than that of the sample prepared by 1 hr annealing with a flat band potential of 0.144 V and a donor density of 9.81x10^{18} cm^{-3}. This is indicative of an anodic shift with increased annealing time. The donor densities were similar to those reported by Nyarige *et al.* in 2020 [13]. This anodic shift together with the increased donor density could result in enhanced photocurrent properties due to an improvement in the conductivity.

Table 4.3.2. Donor density and flat band potential of hematite thin films at different annealing temperatures

Sample	**Donor density (x 10^{18} cm^{-3})**	**Flat band potential (V)**
30 mins	2.30	0.111
1 hr	9.81	0.144

4.3.7 Linear Scanning Voltammetry analysis

A VersaSTAT 3F potentiostat was used to perform photoelectrochemical measurements. From this the photocurrent density was found using an Ag/AgCl reference electrode, a platinum (Pt) mesh counter electrode and a hematite thin film as the working electrode. An AM 1.5 G xenon (Xe) solar irradiator was used to illuminate the 0.49 cm^2 hematite thin film. The electrolyte used was 1 M sodium hydroxide (NaOH). Linear scanning voltammetry was performed in a cappuccino cell under dark and illuminated conditions. A voltage range of 0 to 1 V was used at a scan rate of 50 mVs^{-1}. The results were plotted and presented in figure 4.3.7.

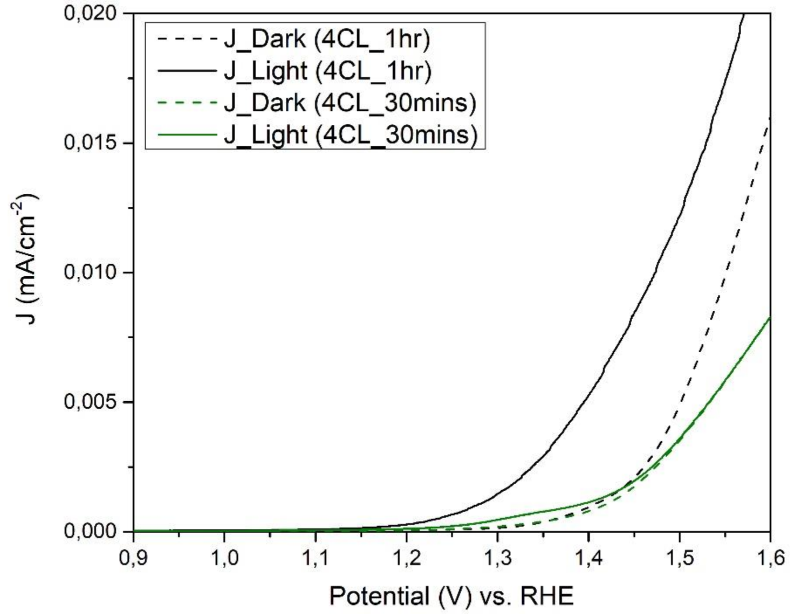

Figure 4.3.7. Photocurrent density of hematite thin films prepared at 30 mins and 1 hr of annealing.

A cathodic shift was observed as the annealing time increased from 30 mins to 1 hr. Additionally, the photocurrent densities were recorded at 1.23 eV vs. RHE as 1.65 x 10^{-4} Acm^{-2} and 4.77 x 10^{-4} Acm^{-2} as annealing time changed from 30 mins to 1 hr. Nyarige *et al.* and Kyesmen *et al.* reported similar current densities in their work on nanostructured hematite [8, 13, 14]. From this study an increase in annealing time led to a three-fold increase in current density. This was coherent with small grain size, homogeneous polycrystallinity and good absorption in the visible region as reported.

4.4 Layered hematite thin films for the optical and structural properties for photoelectrochemical water splitting

In this study three hematite thin films were prepared by chemical spray pyrolysis. One of which comprised of one single layer (1L_1hr) annealed for 1 hr at 500 °C, the second of which comprised of four single layers (4SL_1hr) of hematite thin film with annealing between each layer and the last comprises of four coherent layers (4CL_1hr) of hematite which was annealed once.

4.4.1 X-ray diffraction analysis

XRD was performed in the 2θ range of 20° and 80° to study the structure of the α-Fe_2O_3 crystalline structure, which confirmed the corundum structure of α-Fe_2O_3. Figure 4.4.1 indicated that both the (104) and (110) dominant peaks for α-Fe_2O_3 were present and indexed at 33.87 º and 35.75 º. Furthermore the (110), (024), (112) and (124) peaks were present which correlates to the JCPDS 33-0664 plot card for α-Fe_2O_3. Furthermore, the high intensity and narrow width of the peaks, confirms the high purity of α-Fe_2O_3. No other iron oxide diffraction peaks were present. The single layer sample produced the wides and least intense peaks while the four single layer annealed four-fold times produced the best intensity and narrowest peaks.

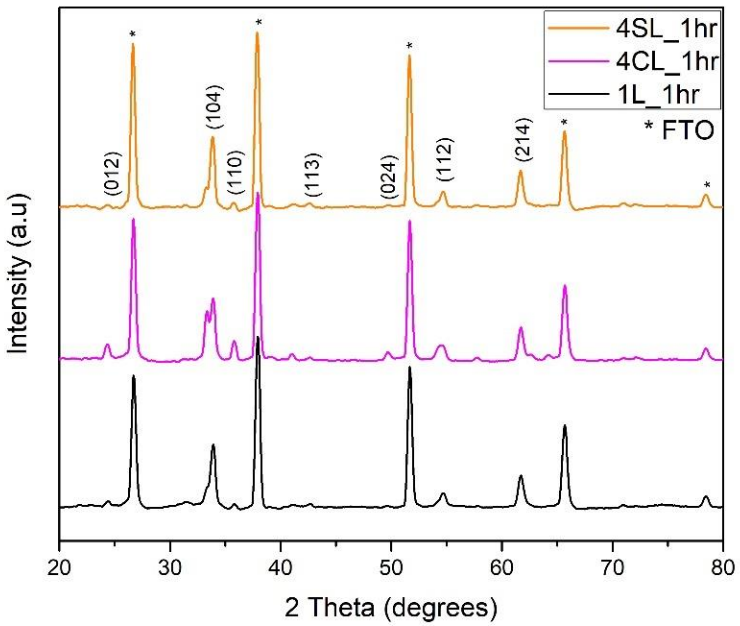

Figure 4.4.1. XRD patterns of α-Fe_2O_3 films synthesized by the formation of one single layer, four coherent layers annealing once and four single layers annealing four times.

The Debye-Scherrer formula together with FWHM calculations from the Origin Pro 9.1 software was used to estimate the crystal sizes for the two dominant (104) and (110) peaks. The average crystal size for the single layer α-Fe_2O_3 film was computed as 17.90 nm whereas the average for the four coherent layers was calculated as 12.91 nm and the average for the four single layers annealed four times was computed as 20.48 nm. The variation in crystallite size could be attributed to the variation in the nanoparticle shapes. The 1L and 4CL thin films showed the best crystallinity.

Table 4.4.1. FWHM and crystallite sizes for the (110) and (104) miller indices for the hematite nanoparticles prepared as one layer, four single layers and four coherent layers.

Sample	Peak	FWHM (°)	2 Theta (°)	Crystal size (nm)
1 L	(104)	0.57	33.87	16.74
1 L	(110)	0.51	35.81	19.06
4 CL	(104)	1.23	33.68	07.78
4 CL	(110)	0.54	35.89	18.05
4SL	(104)	0.48	33.82	19.90
4SL	(110)	0.47	35.74	21.05

4.4.2 Raman spectroscopy

Figure 4.4.2 presents the Raman phonon vibrational modes for hematite. All seven vibrational modes for hematite were present as represented by two A_{1g} at 230 cm^{-1} and 499 cm^{-1} modes and five E_g modes at 251 cm^{-1}, 295 cm^{-1}, 318 cm^{-1}, 409 cm^{-1} and 611 cm^{-1}. The corundum structure for hematite was confirmed by the seven first order vibrational modes at the centre of the Brillouin zone for hematite. The LO and 2LO modes indicating the ferromagnetic properties of hematite were located at 662 cm^{-1} and 1321 cm^{-1}. Furthermore, the single layered sample showed the best intensity and the four single layers annealing four times showed the least intense peaks, this indicates that the crystallinity of both films that were only annealed once were favourable.

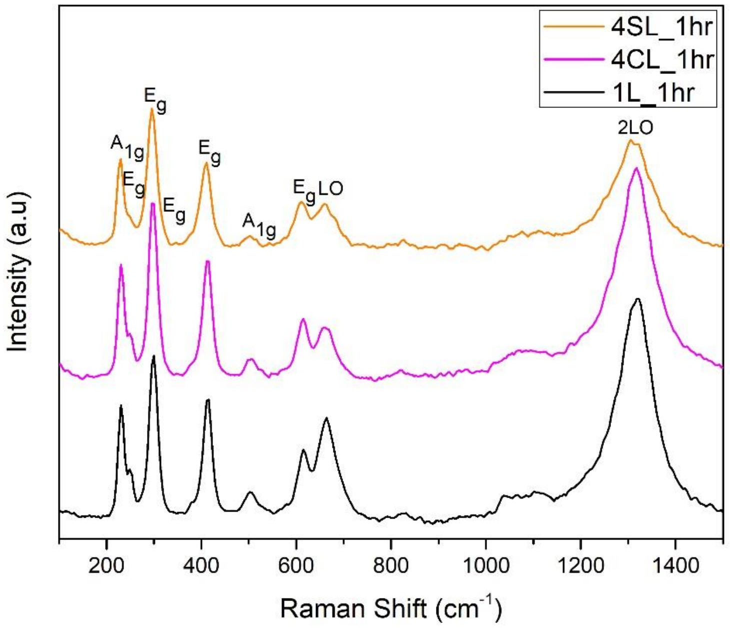

Figure 4.4.2. Raman spectroscopy of α-Fe_2O_3 films prepared as one layer, four single layers and four coherent layers.

4.4.3 Variation in layering with annealing

A cross section under FE-SEM was used to determine the thickness of the α-Fe_2O_3 films. The thickness of the FTO substrate was excluded in the cross-section measurements as presented in figure4.4.3. The single layer was approximately one fourth the thickness of the four layered samples of 240.6 nm which both presented similar thicknesses of 893.2 nm and 870.3 nm.

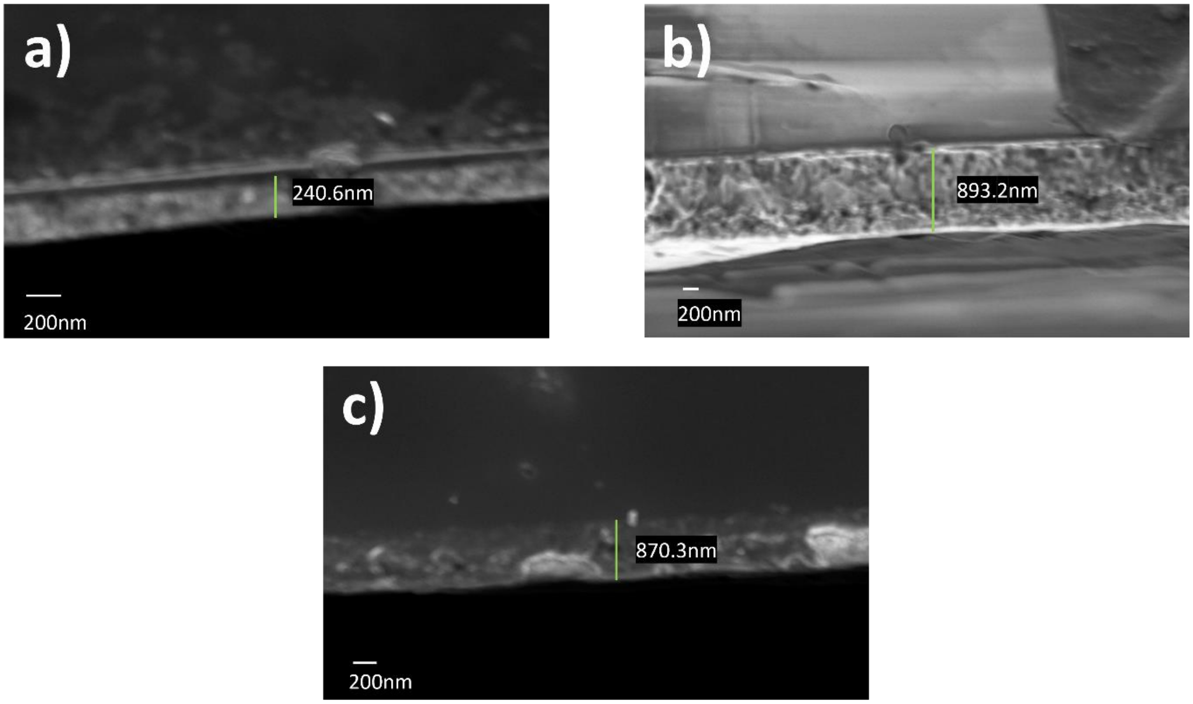

Figure 4.4.3. Cross-sectional micrograph images estimating the thickness using FE-SEM for hematite films synthesized as (a) one layer (b) four single layers (c) four coherent layers.

Additionally, it was found that the sample that was annealed four times presented four individual layers as presented in figure 4.4.4 as opposed to the sample that was annealed once and showed a homogenous layer. Each layer was approximately 200 nm which is expected from the thickness of the single layered sample. These layers were found at 245.6 nm, 468.9 nm, 736.9 nm and 893.2 nm.

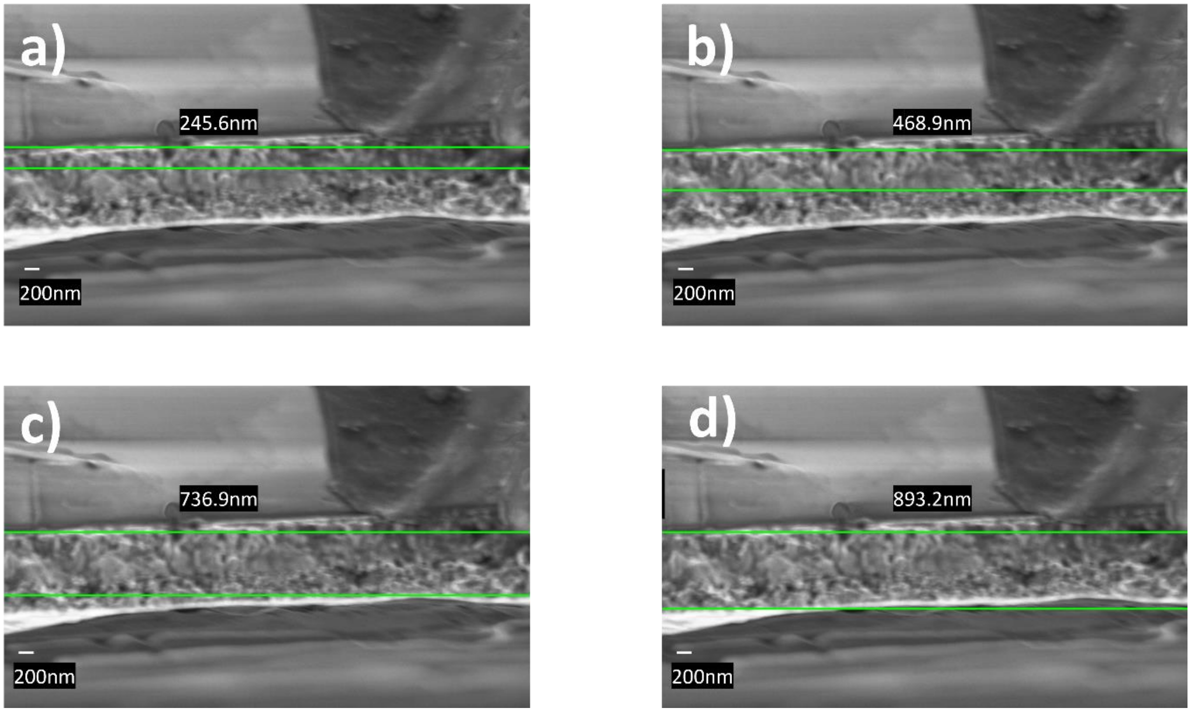

Figure 4.4.4. Cross-sectional micrograph images indicating the layering present in the four single layer thin film.

4.4.4 Surface morphology

The surface morphology of the nanoparticles was observed by FE-SEM. From figure 4.4.5, it is evident that the nanoparticles were in uneven shapes. The single layer thin film presented nanorod-like shapes starting to form, whereas the four single layered sample presented nanorods and some agglomerated nanospeheres. The four coherent layered film presented agglomerated nanospheres. Average grain intercept was used to determine the grain sizing via the Image J software. The grain sizes were determined as 40.76 nm, 35.19 nm and 33.23 nm respectively. The four coherent layered sample presented agglomerated nanospheres with the smallest grain size. Yun *et al.* reported on the effect of nanoparticle shape for PEC water splitting. They found that nanospheres produced more hydrogen due to a significant increase in charge transfer rates [15].

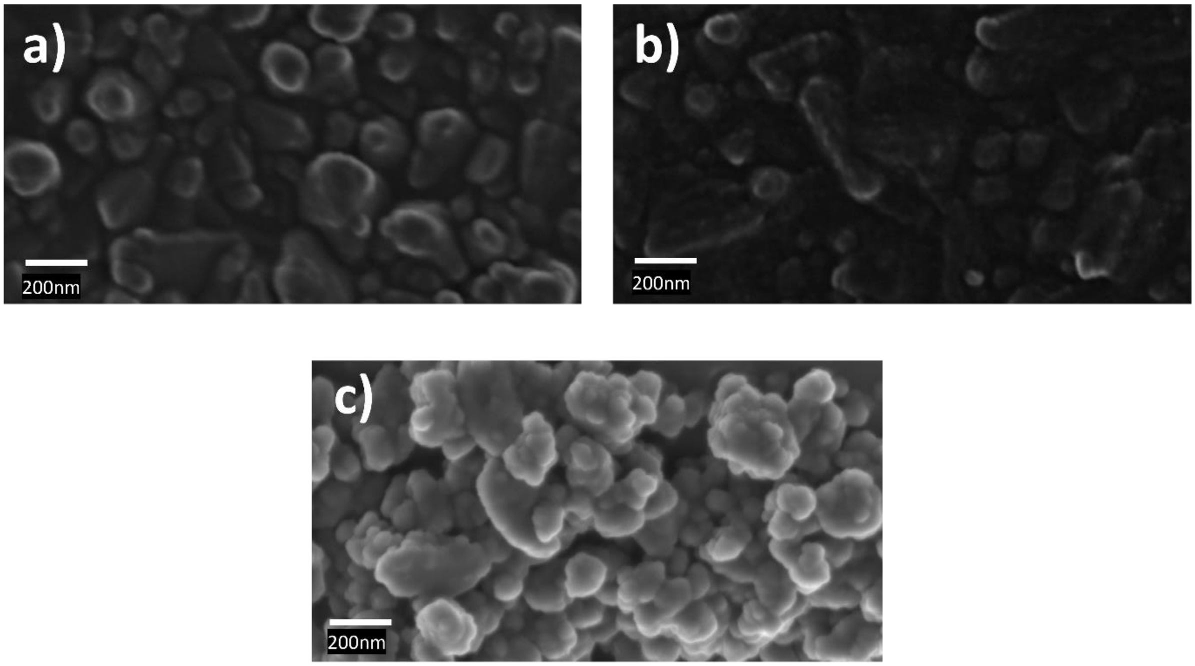

Figure 4.4.5. FE-SEM micrograph images of α-Fe_2O_3 nanoparticles synthesized as (a) one layer (b) four single layers (c) four coherent layers

4.4.5 Optical studies

UV-Vis spectroscopy was performed to measure the onset absorption and bandgap of the α-Fe_2O_3 thin films in the range 400 – 800 nm as show in figure 4.4.6. From these plots the energy bandgaps were estimated as 1.99 eV, 2.0 eV and 1.99 eV. All films were found to have large absorb in the visible spectrum due to their small indirect bandgaps. There was a slight red shift from the single layered sample to the single layered sample, as opposed to the slight blue shift from the coherent layered sample to the single layered sample. These shifts could be attributed to the increased annealing frequency. Both films that were annealed once presented with smaller bandgaps which are favourable.

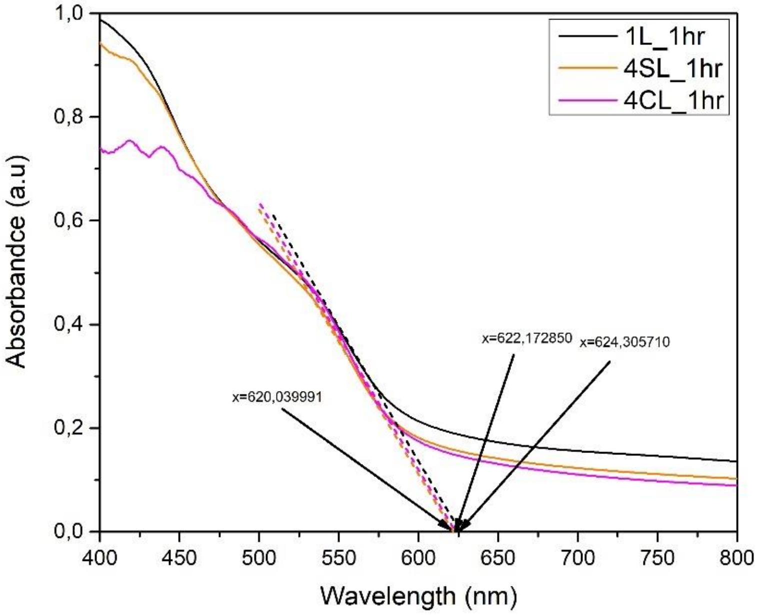

Figure 4.4.6. Absorbance spectra of hematite films prepared as one layer, four single layers and four coherent layers.

4.4.6 Mott-Schottky analysis

The electrical properties of the single layered, three coherent layered and four single layered samples were performed by Mott-Schottky analysis. A 1/capacitance against potential plot, as depicted in figure 4.4.7, was used to calculate the flat band potential and donor density by using the M-S equation. A potential frequency of 10 kHZ was used for all measurements. All three plots presented a positive slope which is indicative of a n-type semiconductor.

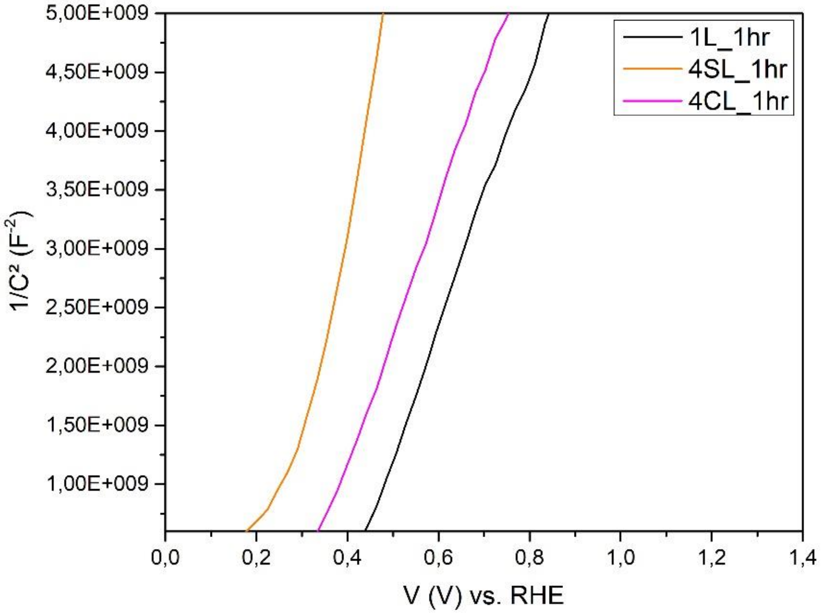

Figure 4.4.7. Mott-Schottky plots of hematite films prepared with one single layer, four single layers and four coherent layers.

The flat band potentials obtained from the M-S analysis were 0.198 V, 0.079 V and 0.144 V vs. RHE respectively for the single layer, four single layers (annealed four times) and four coherent layers (annealed once) samples. This revealed a cathodic shift from the single layered films to the coherent layered film which is indicative of increased conductivity and thus enhanced electrochemical performance. The donor densities were calculated using the Origin Pro 9.1 software as 10.6x10^{18} cm^{-3}, 4.89 x10^{18} cm^{-3} and 9.81 x10^{18} cm^{-3} this indicates that the single layered sample performed best followed by the four coherent layered sample and lastly by the four single layered sample, which is in line with theory as donor density decreases with an increase of film thickness. This also indicates that there is a significant decrease in donor density as annealing frequency is increased.

Table 4.4.2. Summary of the donor density and flat band potential of hematite films prepared with one single layer, four single layers and four single layers.

Sample	**Donor density (x 10^{18} cm^{-3})**	**Flat band potential (V)**
1L_1hr	10.6	0.198
4SL_1hr	4.89	0.079
4CL_1hr	9.81	0.144

4.4.7 Linear Scanning Voltammetry analysis

Linear scanning voltammetry measurements were performed under dark and light irradiation using the VersaSTAT 3F potentiostat workstation. The measurements were performed on the single layer, four single layers and four coherent layered samples. The focus area was 0.49 cm^{-2} and the illumination was performed by a Xe (1 sun) solar simulator. The photocurrent measurements were obtained at 1.23 eV vs. RHE as 4.35 x 10^{-4} Acm^{-2}, 2.26 x 10^{-4} Acm^{-2} and 4.77 x 10^{-4} Acm^{-2} for 1L, 4SL and 4CL respectively.

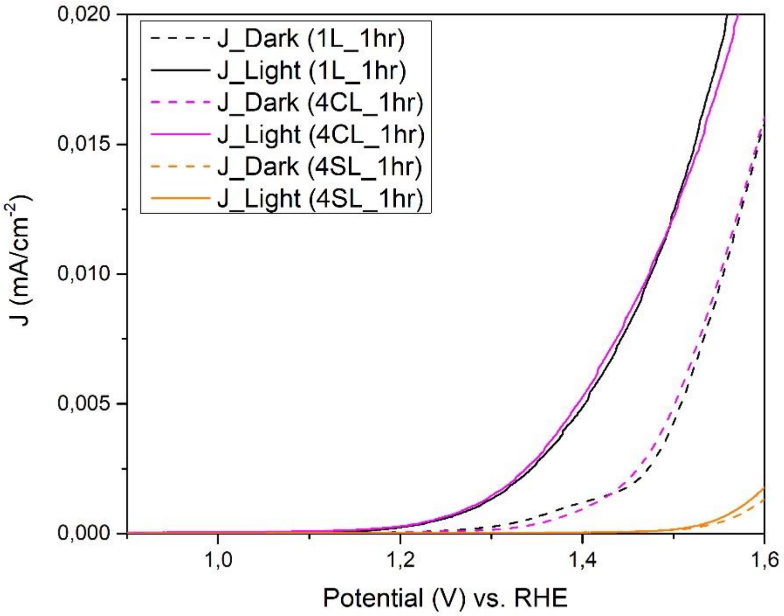

Figure 4.4.8. Photocurrent density of hematite films synthesized with one single layer, four single layers and four coherent layers.

A double-fold increase in photocurrent density was obtained for the single layer and four coherent layered samples which were both annealed once as compared to the four single layered sample which was annealed four-fold. This increase could have resulted from the increased donor density of both films that were annealed once. The improved performance of the single layered film could be attributed to the nanorod structures as reported by Yun *et al.* [15]. The decreased onset absorption, relatively large crystal and grain structures and low IV performance could be indicative of annealing frequency having a negative impact on hematite thin films for PEC water splitting.

References

[1] Kyesmen, P.I., N. Nombona, and M. Diale, *Influence of coating techniques on the optical and structural properties of hematite thin films.* Surfaces and Interfaces, 2019. **17**: p. 100384.

[2] Liu, J., et al., *Highly oriented Ge-doped hematite nanosheet arrays for photoelectrochemical water oxidation.* Nano Energy, 2014. **9**: p. 282-290.

[3] Guo, X., et al., *Synthesis and microwave absorption of uniform hematite nanoparticles and their core-shell mesoporous silica nanocomposites.* Journal of Materials Chemistry, 2009. **19**(37): p. 6706-6712.

[4] Gaviria, J., et al., *Hematite to magnetite reduction monitored by Mössbauer spectroscopy and X-ray diffraction.* Physica B: Condensed Matter, 2007. **389**(1): p. 198-201.

[5] Lagoeiro, L., *Transformation of magnetite to hematite and its influence on the dissolution of iron oxide minerals.* Journal of Metamorphic Geology, 1998. **16**(3): p. 415-423.

[6] Zhu, W., et al., *Monodisperse porous pod-like hematite: hydrothermal formation, optical absorbance, and magnetic properties.* Materials Letters, 2011. **65**(6): p. 1003-1006.

[7] Katsuki, H., et al., *Ultrafast microwave-hydrothermal synthesis of hexagonal plates of hematite.* Materials Chemistry and Physics, 2018. **205**: p. 210-216.

[8] Nyarige, J.S., T.P. Krüger, and M. Diale, *Effects of L-arginine concentration on hematite nanostructures synthesized by spray pyrolysis and chemical bath deposition.* Physica B: Condensed Matter, 2020. **581**: p. 411924.

[9] Neufeld, O., N. Yatom, and M. Caspary Toroker, *A first-principles study on the role of an Al2O3 overlayer on Fe2O3 for water splitting.* ACS Catalysis, 2015. **5**(12): p. 7237-7243.

[10] Glusker, J.P., M. Lewis, and M. Rossi, *Crystal structure analysis for chemists and biologists*. Vol. 16. 1996: John Wiley & Sons.

[11] Maabong, K., et al., *Nanostructured hematite thin films for photoelectrochemical water splitting.* Physica B: Condensed Matter, 2018. **535**: p. 67-71.

[12] Hankin, A., et al., *Flat band potential determination: avoiding the pitfalls.* Journal of Materials Chemistry A, 2019. **7**(45): p. 26162-26176.

[13] Nyarige, J.S., T.P. Krüger, and M. Diale, *Influence of precursor concentration and deposition temperature on the photoactivity of hematite electrodes for water splitting.* Materials Today Communications, 2020. **25**: p. 101459.

[14] Kyesmen, P.I., N. Nombona, and M. Diale, *Effects of film thickness and coating techniques on the photoelectrochemical behaviour of hematite thin films.* Frontiers in Energy Research, 2021. **9**: p. 217.

[15] Yun, H.J., et al., *Effect of TiO2 nanoparticle shape on hydrogen evolution via water splitting.* Journal of nanoscience and nanotechnology, 2011. **11**(2): p. 1688-1691.

[16] López-Sánchez, J., del Campo, A., Román-Sánchez, S., Rodríguez de la Fuente, Ó., Carmona, N. and Serrano, A, *Large two-magnon Raman hysteresis observed in a magnetically uncompensated hematite coating across the morin transition.* Coatings, 2022 **12**(4): p.540.

5 Conclusion and future work

5.1 Conclusion

This work was based on the study of hematite thin films fabricated by various annealing approaches for applications in photoelectrochemical water splitting.

Two colloidal based synthesis techniques namely dip coating and chemical spray pyrolysis were directly compared in section 4.2. The samples were synthesized on fluorine-doped tin oxide substrates for improved conductivity. The transformation from magnetite to hematite took place during annealing for both films as confirmed with XRD. All phases for hematite were present and indexed in both samples and confirmed with Raman spectroscopy. Raman spectroscopy displayed all seven optical vibrational modes for hematite. Additionally, the ferromagnetic properties for hematite were confirmed using the LO and 2LO modes. Furthermore, a decrease was found in the grain size for the dip coating. FE-SEM revealed nanospheres for the DC sample and agglomerated nanodisks, nanorods and nanoparticles for the SP film. Furthermore, AGI revealed smaller particle sizes for the SP sample. UV-Vis revealed the optical bandgaps for both films as 2.08 eV and 2.03 eV for DC and SP respectively. The change in bandgap was attributed to the change in nanoparticle shape. Although both methods have been known for the synthesis of hematite thin films, due to the improved bandgap, small particle size and good crystallinity, chemical spray pyrolysis revealed a possible small advantage.

In section 4.3, a variation in annealing time was used to better understand the effects of annealing time on hematite thin films. XRD indicated better crystallinity and smaller crystallite size as annealing time increased. Furthermore, Raman spectroscopy confirmed the crystallinity and crystal sizing. Additionally, all vibrational Raman modes were present and indexed at their respective wavenumbers. However, FE-SEM cross-section revealed an increase in film thickness with annealing time. Furthermore, FE-SEM revealed a decrease in nanoparticle size and an increase in nanoparticle formation with increased annealing time. UV-Vis indicated a decrease in bandgap with an increase of annealing duration.

This was enhanced by Mott-Schottky analysis under dark conditions which revealed increase in both donor density from 2.30 x 10^{18} cm^{-3} to 9.81 x 10^{18} cm^{-3} and, an increase in flat band potential from 0.111 V vs. RHE to 0.144 V. vs RHE, as annealing time was lengthened. Additionally, LSV measurements under dark and illuminated conditions revealed a two-fold increase from 1.65 x 10^{-4} Acm^{-2} to 4.77 x 10^{-4} Acm^{-2} at 1.32 V vs. RHE as annealing time increased. This was intensified by small grain size, good crystallinity, enhanced solar absorption in the visible spectra and nanostructuring.

Section 4.4 discussed the influence of layering and annealing frequency on pristine hematite nanostructures. XRD analysis confirmed the polycrystallinity of all films with all seven main peaks indexed. Additionally, it revealed that annealing frequency and layering can influence the crystal size, the four coherent layers sample presented the smallest crystal size at 12.91 nm, followed by the single layer film at 17.90 nm and lastly the four single layered sample at 20.48 nm. Raman spectroscopy confirmed all optical and magnetic vibrational modes for hematite was present. Furthermore, it showed a decrease in crystallinity for the four single layered sample, this could possibly be attribute to the increased annealing frequency of this film. FE-SEM cross section confirmed that both four layered films presented a layer thickness in the range of 800 nm whereas the single layer had a thickness in the range of 200 nm. Furthermore, it clearly showed the layer formation when annealed between every layer formation. FE-SEM revealed homogenous surface morphology for all three films, with the formation of nanorods on both the single layer and single layered samples versus an agglomeration of nanospheres on the coherent layered film. Additionally, FE-SEM revealed an increase in particle size of ~ 5-10 nm with an increase of annealing frequency. Mott-Schottky analysis showed a decrease in donor density from 0.198V vs. RHE to 0.144 V vs. RHE for the single layer film versus the coherent layered film and a further decrease to 0.079 V vs. RHE for the single layered film. Similarly, M-S analysis also depicted a decrease in donor density with layering and annealing frequency. This was further enhanced by LSV measurements which revealed photocurrent measurements of 4.35 x 10^{-4} Acm^{-2}, 2.26 x 10^{-4} Acm^{-2} and 4.77 x 10^{-4} Acm^{-2} at 1.23 eV for 1L, 4SL and 4CL respectively. This was strengthened by the good absorption, crystallinity, and small grain sizing of both the single layer and coherent layered nanostructures.

5.2 Future work

In this study hematite thin films were successfully synthesized, and their optical, structural, and electrochemical properties were characterized for PEC water splitting. It was found that annealing time and frequency could potentially influence the optical, structural, and electrochemical properties of hematite. Early results showed that the coating technique could have an influence on the PEC performance of hematite, more comparative studies are needed to fully comprehend which methods would be most beneficial. Furthermore, more work needs to be done in understanding the processing parameters of dip coating and spray pyrolysis, viscous drag, withdrawal rate, drying time, spray rate, spray height and spray time are only some of the variations that can be studied in these techniques. Furthermore, from the results in this study, annealing temperatures and elongated times can also be beneficial to research. Similarly, studies on the variation of film thickness could also possibly result in a variation in electrochemical performance. Additional studies could also include the effect of various nanostructure size and shapes on the PEC performance of hematite. We trust that the aforementioned enhancement studies could lead to future increases in the PEC performance of hematite thin films.